J. Fluid Mech. (2008), *vol.* 601, *pp.* 281–315.
doi:10.1017/S0022112008000694 Printed in the United Kingdom

Measurements of the velocity field of a wing-tip vortex, wandering in grid turbulence

S. C. C. BAILEY† AND S. TAVOULARIS

University of Ottawa, Department of Mechanical Engineering, 161 Louis Pasteur, Ottawa, Ontario, K1N 6N5, Canada
stavros.tavoularis@uottawa.ca

(Received 22 May 2007 and in revised form 15 January 2008)

Velocity measurements were performed in a wing-tip vortex wandering in free-stream turbulence using two four-wire hot-wire probes. Vortex wandering was well represented by a bi-normal probability density with increasing free-stream turbulence resulting in increased amplitude of wandering. The most dominant wavelength of wandering was found to remain unaffected by free-stream conditions. Two-point velocity measurements were used to reconstruct the vortex velocity profile in a frame of reference wandering with the vortex. Increasing turbulence intensity was found to increase the rate of decay of the vortex peak circumferential velocity while the radial location of this peak velocity remained unchanged. These results are consistent with several possible vortex decay mechanisms, including the stripping of vorticity by azimuthally aligned vortical structures, transfer of angular momentum from the vortex to these structures during their formation and the deformation and breakup of the vortex by strong free-stream eddies.

1. Introduction

Vortices are encountered in a wide variety of fluid systems, ranging in scale from hurricanes and tornadoes to those shed by self-propelled micro-organisms. Of significant engineering importance are the vortices that roll up around the tips of finite-span lifting surfaces, such as wings and propellers. The trailing vortices of flying airplanes have long been known to create serious hazards, if they intersect the flight paths of other aircraft. Wing-tip vortices exhibit strong stability and slow decay rates and, therefore, their interference with oncoming flights persists over long distances and times. In this respect, atmospheric turbulence has a beneficial effect, as it is known to enhance the vortex rate of decay (Sarpkaya & Daly 1987), thus providing motivation for the study of vortices in turbulent streams. Moreover, studying the interaction of an isolated vortex and a turbulent stream can contribute towards understanding turbulence dynamics as well, because vortical coherent structures are essential elements of turbulent shear flows. Despite the importance of this issue, there have been surprisingly few experimental studies of the effects of externally introduced vortices on adjacent turbulent eddies.

One important question when considering decay of a vortex is the degree to which vorticity diffuses due to turbulence in the vortex core. Such turbulence could be

† Present address: Department of Mechanical and Aerospace Engineering, Princeton University, Princeton, NJ 08544, USA.

entrained in the vortex core during formation (Spalart 1998), or transferred from turbulence in the surroundings through exchange of core fluid and free-stream fluid (Bandyopadhyay, Stead & Ash 1991). Squire (1965) modelled the diffusion of a turbulent vortex by using an eddy viscosity proportional to the vortex circulation; however, Chow, Zilliac & Bradshaw (1994) found that the turbulence structure is poorly represented by an isotropic eddy viscosity model. Additionally, Chow *et al.* (1994) suggested that a turbulent vortex core would rapidly relaminarize due to the stabilizing effects of streamline curvature (Bradshaw 1969). Cotel & Breidenthal (1999) further modelled this process and found that the core motion is very stable and that small-scale external perturbations were unable to penetrate the core. Jacquin & Pantano (2002) noted that, for sufficiently strong circumferential velocity relative to the streamwise velocity deficit, perturbations within the vortex core would be dispersed by inertial waves before they could grow. Experimental evidence of a laminar core can be found in the measurements of Devenport *et al.* (1996), which show little or no velocity fluctuations within the vortex core.

Despite the inherent stability of the vortex core, in the presence of a strong streamwise velocity excess or deficit along the vortex axis, the vortex would be susceptible to a variety of instabilities, including viscous instabilities (Fabre & Jacquin 2004) and transient growth (Heaton & Peake 2007). Within a turbulent free stream, a vortex could be susceptible to elliptic instabilities (Lacaze, Ryan & Le Dizès 2007) caused by the external strain field, or energy could be transferred into the vortex core through critical layer waves (Fabre, Sipp & Jacquin 2006). Experimental evidence for the presence of turbulence within the vortex core has been given by Green & Acosta (1991), who observed unsteadiness in the core, Sarpkaya & Daly (1987), who observed an increase in the rate of decay of trailing vortex pairs surrounded by grid turbulence, and Bandyopadhyay *et al.* (1991), who observed an intermittent exchange between core fluid in an isolated vortex and fluid in a turbulent free stream. Bandyopadhyay *et al.* (1991) also observed that the turbulent fluid drawn into the vortex core became relaminarized. Using particle image velocimetry and two different turbulence-producing grids, Heyes, Jones & Smith (2004) observed that, although in the near field the vortex decayed more rapidly as the free-stream turbulence increased, in the far field the rates of decay in the turbulent free-streams were indistinguishable from that in the laminar free-stream case. Heyes *et al.* (2004) concluded that the free-stream turbulence altered vortex formation and roll-up, but had no effect on the fully formed vortex. In contrast, Bailey, Tavoularis & Lee (2006) observed that the free-stream turbulence had little effect on the wing-tip vortex formation process, noting only the introduction of additional unsteadiness into the vortex.

Additional insight into the interactions between a vortex and a turbulent free stream has been provided by numerical studies using direct numerical simulations and large-eddy simulations. Melander & Hussain (1993) observed that the azimuthal strain imposed by the vortex resulted in stretching the initially non-coherent surrounding turbulent eddies, thus accentuating the azimuthal component of vorticity. This process facilitated pairing of eddies with similar sense of rotation into growing secondary coherent structures, arranged in spirals around the vortex. Coherent structures with both senses of azimuthal vorticity were observed, which were aligned accordingly in the spiral. The structures evolved rapidly, within two turns of the vortex (Miyazaki & Hunt 2000). Melander & Hussain (1993) also investigated the influence of free-stream fluctuation levels: for low fluctuation levels, coherent structures would form, but they would decay downstream, leaving the vortex nearly unaltered; at moderate fluctuation levels, turbulence was sustained in the secondary structures and the vortex

coexisted with these structures; at sufficiently high free-stream turbulence levels, bending waves were induced in the vortex, which corrupted the axisymmetry of the secondary structures; when free-stream turbulence exceeded some level, the vortex was destroyed (in agreement with Holzäpfel *et al.* 2003).

Numerical studies of Holzäpfel *et al.* (2003) and Takahashi, Ishii & Miyazaki (2005) found that free-stream turbulence enhanced vortex decay and Melander & Hussain (1993) observed an increased rate of dissipation of turbulent kinetic energy in the vicinity of the secondary structures. Holzäpfel *et al.* (2003) suggested that, during their formation, the secondary structures extracted rotational energy from the vortex, but, once fully formed, had little effect on vortex circulation. Marshall & Beninati (2000) hypothesized that vortex decay was the result of core vorticity stripping by counter-rotating secondary structures (Marshall 1997); however the DNS study of Marshall & Beninati (2005) found little direct evidence for such a mechanism, except during vortex breakup by strong turbulence. Finally, free-stream turbulence has been observed to excite bending modes in the vortex (Takahashi *et al.* 2005), which may induce additional turbulence production within the core (Pradeep & Hussain 2006).

Vortex bending and the associated random transverse motion of the vortex about its average path are well known phenomena, which have been observed in both turbulent and non-turbulent streams and are referred to as vortex wandering or meandering. Wandering in non-turbulent wind-tunnel flows has been attributed to (even low level) background flow fluctuations (Corsiglia, Schwind & Chigier 1973; Baker *et al.* 1974; Devenport *et al.* 1996), intermittent exchange of core fluid with free-stream fluid (Green 1995), self-induced Biot-Savart induction (Rokhsaz, Foster & Miller 2000), Biot-Savart induction from Kelvin–Helmholtz vortices forming in the shear layers of the vortex generator (Gursul & Xie 1999), interactive instabilities between the trailing vortex and other vortices in the flow (Jacquin *et al.* 2001), vibration of the vortex generator (Jacquin *et al.* 2001) and the excitation of Kelvin waves within the vortex by turbulence external to it (Fabre & Jacquin 2004). Wandering amplitude increases with streamwise distance (Rokhsaz *et al.* 2000; Devenport *et al.* 1996).

Vortex wandering introduces appreciable complications in experimental studies of vortices, especially when attempting to measure velocity in the vortex core using fixed probes. Devenport *et al.* (1996) used an analytical approach to determine the magnitude of vortex wandering and to correct their hot-wire measurements. They found that errors in time-averaged measurements due to wandering were significant only within the vortex core, and that wandering occurred in a broadband, low-frequency range. The validity of this approach was confirmed by Heyes *et al.* (2004), who studied a trailing vortex in free-stream turbulence using particle image velocimetry. Beninati & Marshall (2005) were able to isolate the effects of free-stream turbulence from effects of wandering due to wind tunnel unsteadiness and model vibration, by using a specially designed, low-disturbance, vortex generator. They noted that turbulence-induced bending waves in the vortex had a wavelength compatible with the spacing of azimuthally aligned turbulent structures observed in the numerical simulations of Marshall & Beninati (2005) and concluded that it is these structures that induce bending waves into the vortex.

The objective of the present study is to investigate experimentally the effects of free-stream turbulence on the development of a wing-tip vortex in the near field (within ten chord lengths) of the wing. Besides a low-turbulence case, used for comparisons, two free-stream turbulent grids were used to generate two different sets of turbulent free-stream conditions. The resulting velocity fields were measured in five transverse planes downstream of the wing using single-point and two-point

four-wire probe measurements. Analytical procedures were developed to quantify vortex wandering and to reconstruct the average velocity profile of the vortex in a frame of reference wandering with the vortex. Earlier parts of this work have been presented by Bailey *et al.* (2006), who examined the influence of free-stream turbulence on vortex formation and reported time-averaged streamwise and circumferential velocity measurements in both non-turbulent and turbulent free streams.

2. Experimental facilities, instrumentation and procedures

2.1. *Apparatus*

Experiments were conducted in an open circuit, suction-type wind tunnel, having a test section with dimensions $0.6\,\mathrm{m} \times 0.9\,\mathrm{m} \times 4.3\,\mathrm{m}$. The velocity in the core of the tunnel test section varied by less than 1 % of the centreline speed. In the absence of the wing, velocity fluctuations were also nearly uniform in the core of the test section. The standard deviation of velocity fluctuations 0.61 m downstream of the test section entrance was about 0.2 % of the free-stream velocity, increasing to about 0.3 % at the end of the test section. Free-stream velocity was found to remain within 2 % over several hours.

The main test section was equipped with an automated streamlined two-axis traversing system with a positioning resolution of 0.005 mm per step. The traversing system had a probe holder mounted at the end of a sting allowing a four-wire probe to be mounted on the traverse with its measurement volume 0.360 m upstream of the traverse body.

For two-probe measurements, a specialized probe holder was mounted at the end of the sting, designed to allow accurate adjustment of their transverse separation. Springs were incorporated in the device to minimize lead screw backlash by providing positive force on the threads. Utilizing a lead screw with a 0.5 mm pitch, the manually operated traverse had a positioning accuracy of approximately 0.05 mm. The probe holder was designed to allow a minimum probe separation of 7.1 mm, which was the lowest possible value permitted by the probe body thicknesses. The maximum possible probe spacing, set by the length of the lead screw, was 27.6 mm.

The vortex was generated by a wing with a NACA0012 symmetric profile, machined from an aluminium block. The wing had a rectangular planform with a semi-span $b = 0.5207\,\mathrm{m}$ and a chord $c = 0.1778\,\mathrm{m}$ and a plane tip with sharp edges. Its root was mounted on a circular endplate with a diameter 0.318 m, positioned 38.1 mm above the tunnel floor and having a bevelled edge to minimize the interaction with the wind-tunnel boundary layer. The wing angle of attack could be changed using a rotary table mounted underneath the wind tunnel with the axis of rotation passing through the profile's aerodynamic centre (quarter-chord point). The wing was mounted through the floor of the wind tunnel such that its quarter-chord axis was along the centreline of the wind tunnel, 1.37 m downstream from the end of the contraction. A boundary layer trip wire of diameter 0.58 mm was attached on the suction surface, $0.10c$ away from the leading edge, to induce transition, thus reducing the possibility of separation and sensitivity to free-stream conditions.

Free-stream turbulence was generated using two square-mesh perforated plates ('grids'). Both had square openings punched out from 3.175 mm thick aluminium plates and identical solidities of 0.44. The 'small grid' had a mesh size $M = 25.4\,\mathrm{mm}$, whereas the 'large grid' had $M = 50.8\,\mathrm{mm}$. The measurements presented in this report were performed either with no grid in place or with one grid located 0.76 m upstream of the wing quarter-chord axis. Characterization of the grid turbulence was also

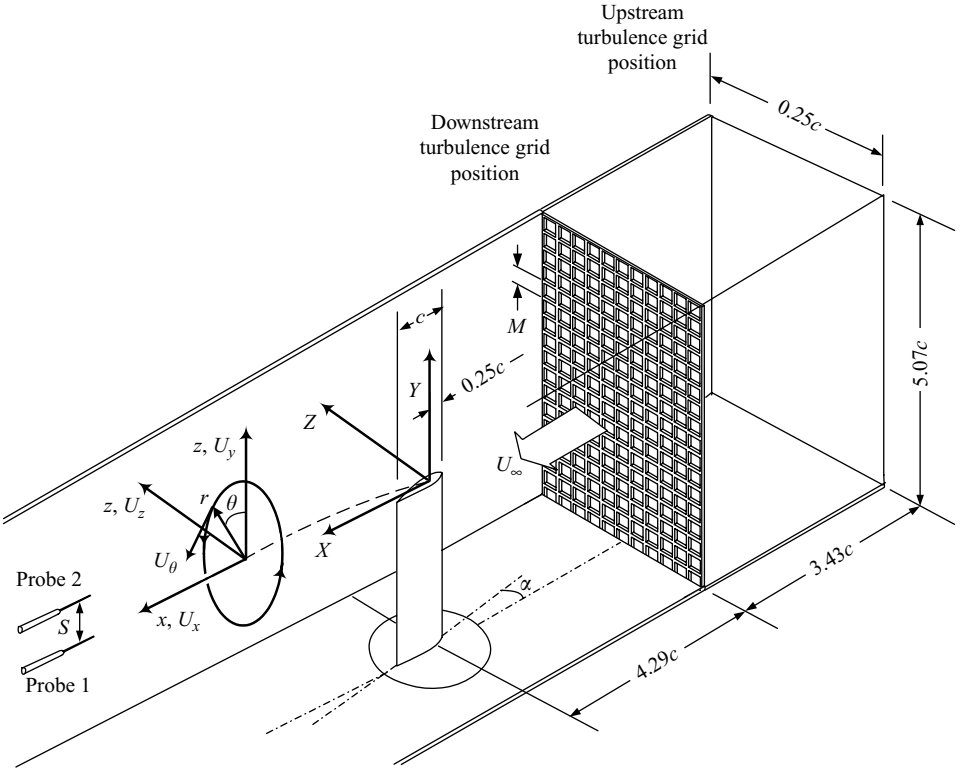

FIGURE 1. Sketch of the experimental arrangement illustrating the coordinate system.

performed with each turbulence grid located 1.37 m upstream of the wing quarter-chord point. Measurement cases with the small grid or large grid in the upstream location are referred to as the 'small-grid-upstream' and 'large-grid-upstream' cases respectively.

A sketch of the experimental setup is shown in figure 1. It illustrates the coordinate systems, nomenclature and some of the important dimensions used in the experiments. A wing-based, fixed Cartesian coordinate system X, Y, Z was defined such that its origin coincided with the quarter-chord point of the wing at the tip. The downstream location of each measurement plane was specified by X and the vertical direction by Y. Moreover, Cartesian (x, y, z) and cylindrical (x, r, θ) coordinate systems were defined on each measurement plane such that their origin moved along the time-averaged axis of the vortex, the x-axis was tangential to the vortex axis and the y-axis was always vertical. In all reported cases, the inclination of the x-axis with respect to the X-axis was less than 5°. When two probes were used in the experiments, they were positioned such that their measurement volumes were separated by a distance S parallel to the Y-axis and were both located on the same streamwise plane.

2.2. *Instrumentation*

Two custom-built, four-sensor, modified Kovasznay-type hot-wire probes were used to measure the instantaneous, local velocity vector, both in magnitude and in direction. The principal probe used in this investigation (probe 1) had a measurement volume of dimensions $0.68 \times 0.68 \times 0.46$ mm. Sensors were made from 2.5 μm Platinum-10 % Rhodium wire welded onto the probe prongs and had a length of approximately

0.66 mm. The sensing wires for this particular probe were inclined at angles of approximately 4° with respect to the probe axis. Effective sensor angles, determined by directional calibration, were found to be approximately 40°, with slight variations among sensors. The second four-sensor hot-wire probe used (probe 2) had a slightly smaller measurement volume than that of probe 1, with dimensions of approximately $0.5 \times 0.5 \times 0.5$ mm In probe 2, one pair of opposing sensors had effective angles of approximately 40° whereas the other pair had angles of about 50°. Although this asymmetry introduced a reduced measurement acceptance range for certain flow angles (Vukoslavčević, Petrovic & Wallace 2004), it is not a reason for concern in any of the presented measurements.

The free-stream velocity U_∞ was measured by a third hot-wire probe, having a single Platinum–10 % Rhodium sensor, 5 μm in diameter and 2 mm long. This sensor was located 0.3 m upstream of the wing and 0.1 m away from the wall, with the sensing wire parallel to the Y-axis.

Free-stream temperature was monitored using a calibrated thermistor with a 5 s time constant. The thermistor was located at the same streamwise position, but on the opposite side of the wind tunnel, as the hot wire used to measure U_∞.

All hot-wire probes were powered by constant-temperature anemometer circuits (A.A. Labs, Model AN-1003). The probe frequency response of all sensors was determined to be uniform up to at least 40 kHz. The four-wire probe signals were recorded using an 8-channel simultaneous sample-and-hold data acquisition system (UEI PowerDaq PD2-MFS-8-300/16) and the wind-tunnel temperature and free-stream velocity were recorded using a second data acquisition system (IOtech DaqBoard/2000).

In the earlier stages of the investigation, single-point measurements of the grid turbulence (in the absence of the wing) were performed using probe 1 between $X/c = -2.25$ and $X/c = 12.75$ at intervals of $1c$ for the no-grid, small-grid, small-grid-upstream, large-grid and large-grid-upstream cases. The anemometer signals were low-pass filtered at a 3 dB cutoff frequency of 8.2 kHz and digitized simultaneously at a rate of 20 kHz with 15 s long records acquired at each measurement location. Two-point velocity measurements were conducted on planes with $X/c = 3.75$, 5.75, 7.75 and 9.75 for the no-grid, small-grid, and large-grid cases. The signals were low-pass filtered at 14 kHz and digitized at a rate of 30 kHz. Each set of two-probe measurements was performed in two phases. In the first phase, the two probes were separated in the Y-direction by the minimum achievable spacing $S_{\min} = 7.1$ mm and measurements were performed on each measurement plane with high spatial density near the time-averaged vortex axis. Records 15 s long were acquired at each measurement location. These results were used to determine precisely the time-averaged vortex axis. Subsequently, probe 1 was positioned on the time-averaged vortex axis and probe 2 was traversed in the range $7.1 \leqslant S \leqslant 27.6$ mm at 0.5 mm increments. Records of such measurements 180 s long were acquired in each case.

2.3. *Procedures*

All sensors were calibrated for flow velocity *in situ* vs. readings of a Pitot-tube/wall-tap combination before and after each run. Calibration data were fitted by a modified King's Law (Tavoularis 2005) and corrected for mean flow temperature variations (typically less than 1 °C). Velocity magnitude and direction were determined from measured voltages using the lookup-table data reduction technique described by Wittmer, Devenport & Zsoldos (1998), which was capable of determining flow angles within an acceptance cone of at least 30° for probe 1 and, for probe 2, within an

acceptance cone between 22° and 28°, depending on the orientation of the velocity vector with respect to the probe body. For the rare cases for which the flow angle was found to be outside this cone, the velocity was determined using the method of Döbbeling, Lenze & Leuckel (1990). The number of data points requiring this treatment was found to be statistically insignificant. All directional calibrations were performed using an automated, motorized, two-degree-of-freedom calibration jet.

Velocity measurements on each measurement plane are presented with respect to the time-averaged vortex axis (figure 1). Pre-processing of the recorded velocity time series on each measuring plane was performed to account for misalignment of the probe axis x_p and the x-axis. As an initial step, the two time-averaged velocity components $\overline{U}_{y_p}$ and $\overline{U}_{z_p}$ on the plane transverse to x_p were determined. Isocontours of the time-averaged velocity magnitude $(\overline{U}_{y_p}^2 + \overline{U}_{z_p}^2)^{1/2}$ were inspected and, in general, were found to deviate slightly from circular shapes. Then, coordinate transformation to the x, y, z system was applied such that the resulting isotachs $(\overline{U}_y^2 + \overline{U}_z^2)^{1/2}$ were as circular as possible. Typical angles of rotation of the x- and z-axes were less than 5°.

The velocity measurements were normalized by the local free-stream velocity U_o on the corresponding measurement plane. Because of blockage by the wing and its wake, U_o was slightly higher (by up to 5 %) than the undisturbed free-stream velocity U_∞.

2.4. *Uncertainty*

A source of uncertainty is introduced by the elaborate calibration process of the four-wire probes, particularly by the curve-fitting of calibration data and by the conversion of measured cooling velocities to Cartesian velocity components. Unfortunately, quantifying this uncertainty is not a trivial task. Following Wittmer *et al.* (1998), uncertainties in the data reduction technique were estimated by comparing the Cartesian velocity components measured by the probe to those calculated from the calibration jet velocity and probe orientation. For flow angles less than 30°, the maximum uncertainties determined using this technique and a 95 % confidence interval (Tavoularis 2005) were found to be approximately 1.1 % for U_x/U_∞, 1.0 % for U_y/U_∞ and 0.8 % for U_z/U_∞, with the highest uncertainty occurring at larger flow angles.

The uncertainty in streamwise position X/c was 3 %. The uncertainties in relative spatial positions y/c and z/c within a measurement plane, due to the finite size of the probe, were 0.3 %. The uncertainties in absolute spatial positions Y/c and Z/c, caused by reinsertions of the probe in the wind tunnel, were 1 %. The uncertainty in probe separation S, due to imperfections in the lead screw on the probe holder, was 0.05 mm.

A concern when using hot-wire probes is the possibility of flow distortion caused by the intrusiveness of the technique. Using flow visualization, Devenport *et al.* (1996) found that a four-wire probe with dimensions nearly identical to those used in this study did not cause measurable disturbances within the vortex core. Probe-induced disturbances in the present tests should be even lower than those in Devenport *et al.*'s tests, because the present measurements of intensity of the streamwise velocity fluctuations in the vortex core was found to be 40 % lower than that in Devenport *et al.*'s study at the same streamwise position and wing angle of attack, although at different Re_c and aspect ratio (Bailey *et al.* 2006).

Possible probe interference was of particular concern for the two-point measurements. To test this possibility, probe 1 was used to obtain measurements in the vortex for the no-grid case at $X/c = 9.75$, first with probe 2 in place and later without

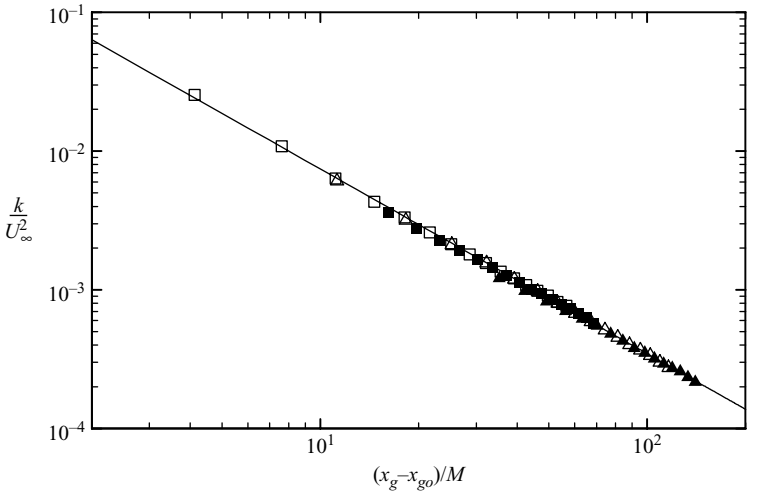

FIGURE 2. Streamwise development of turbulent kinetic energy measured downstream of the present grids with the wing removed from the wind tunnel for small-grid-upstream (▲), small-grid (△), large-grid-upstream (■) and large-grid (□) cases. Solid line indicates power-law fit using equation (3.1).

it. No significant difference was observed between the two sets of time-averaged measurements.

Another test was performed to investigate the possible effect of changing the separation distance of the two probes, due to possible changes in the local pressure field around the probe holder, minor changes in the orientation of probes occurring during the process of changing the probe separation, or slight deformation of the probe holder mechanism caused by rearranging the weight distribution. By examination of measurements obtained with probe 1 fixed in space and probe 2 positioned at different separations, it was observed that the apparent average flow angle measured by probe 1 changed by less than 3°. Such low levels of disturbance are not expected to have a significant effect on the results.

3. Flow conditions

In all reported cases, the angle of attack was set at $\alpha = 5^\circ$ and the wind-tunnel speed was set at $U_\infty = 20\,\mathrm{m\,s^{-1}}$, which corresponds to a wing Reynolds number $Re_c = U_\infty c/\nu = 2.4 \times 10^5$. The effective angle of attack, estimated using the general downwash blockage correction of Rae & Pope (1984), was 5.6°.

To characterize the free-stream conditions generated by each grid, three-component velocity measurements of the grid turbulence were performed with the wing removed from the wind tunnel. Velocity measurements were taken with probe 1 at $U_\infty = 20\,\mathrm{m\,s^{-1}}$ along the centreline of the wind tunnel at streamwise locations between $X/c = -2.25$ and $X/c = 12.75$ at intervals of $1c$ for the small-grid-upstream, small-grid, large-grid-upstream and large-grid cases.

In agreement with previous grid turbulence studies (Pope 2000), the turbulent kinetic energy k, shown in figure 2, was found to decay according to the power law

$$\frac{k}{U_\infty^2} = 0.153\left(\frac{x_g - x_{go}}{M}\right)^{-1.32} \tag{3.1}$$

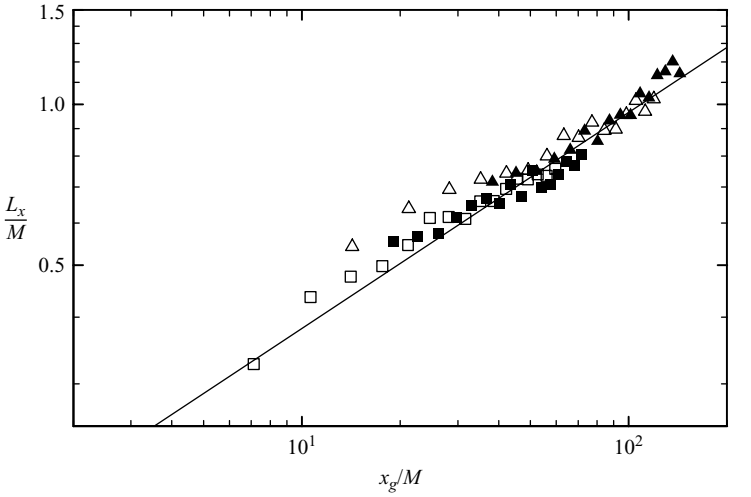

FIGURE 3. Streamwise development of L_x/M as a function of x_g normalized by M for each of the grid turbulence cases without the wing in the wind tunnel for small-grid-upstream (▲), small-grid (△), large-grid-upstream (■) and large-grid (□) cases. Solid line indicates a slope of 0.4.

where x_g is the streamwise distance from the grid and $x_{go} = 3M$ is a 'virtual origin' of the turbulence.

For all cases, the streamwise Reynolds stress was found to be approximately 25 % higher than the horizontal transverse stress and 15 % higher than the vertical one. The stronger level of streamwise fluctuations, compared to those of the transverse ones, is a well-known property of grid turbulence (e.g. Comte-Bellot & Corrsin 1966 used a contraction downstream of the grid to reduce the turbulence anisotropy). The inequality of the two transverse stresses could be, at least partially, attributed to the effective contraction along the wind-tunnel test section caused by boundary layer growth and to the differences in the boundary layers along the horizontal and vertical walls because of the differences between the height and the width of the wind-tunnel test section.

The magnitudes of the length scales within the free stream could play an important role in the interaction between the turbulence and the vortex. The measured evolutions of the longitudinal integral length scales L_x (estimated by integrating the corresponding autocorrelation functions to their first zero crossings) are plotted in figure 3 for each of the cases.

In all cases, the integral length scale increased with streamwise distance. Figure 3 indicates that L_x grew in proportion to $x_g^{0.4}$, in agreement with measurements by Sreenivasan *et al.* (1980).

4. Vortex wandering

4.1. *Correction of Devenport* et al. *(1996)*

Devenport *et al.* (1996) devised an iterative technique to estimate the wandering amplitude and recover the velocity profile in the wandering frame using time-averaged, single-point measurements. In the present context, this technique requires fitting a

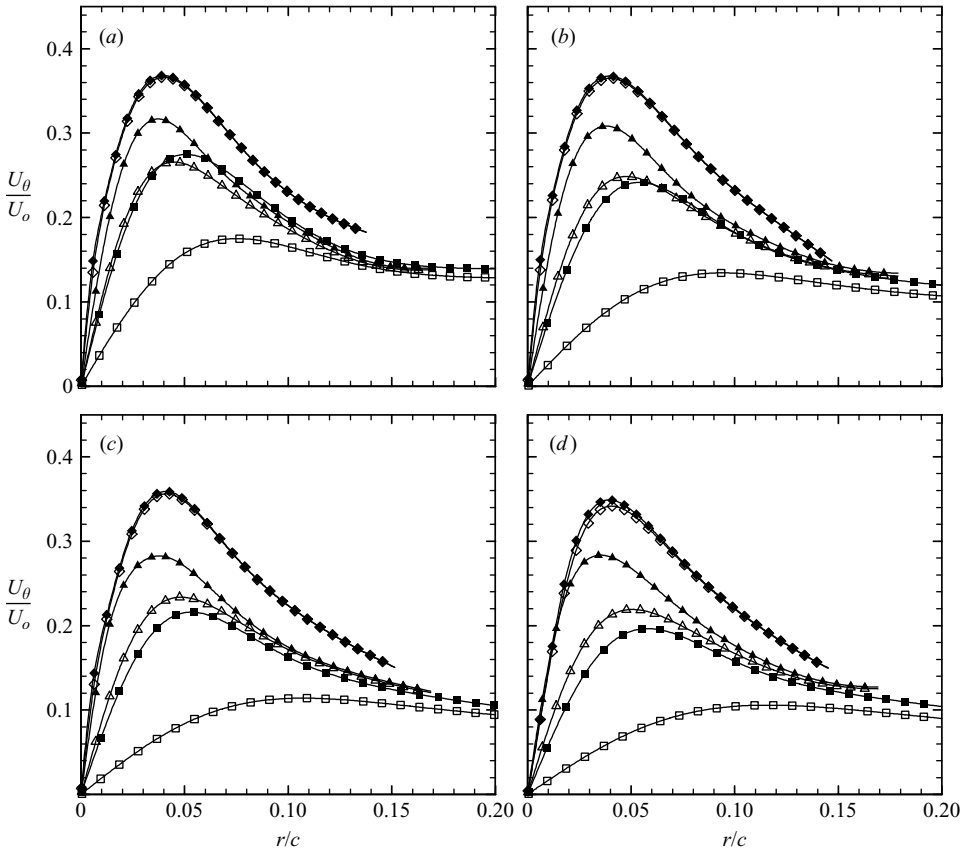

FIGURE 4. Time-averaged radial profiles of circumferential velocity, fitted by equation (4.1) (hollow symbols), and the corresponding corrected profiles (solid symbols) for the no-grid (◇), small-grid (△) and large-grid (□) cases; (*a*) $X/c = 3.75$, (*b*) 5.75, (*c*) 7.75 and (*d*) 9.75.

series of the form

$$U_\theta(0, z) = \sum_{i=1}^{n} \frac{D_i}{z}\left[1 - \exp\left(\frac{-z}{c_i^2}\right)\right] \tag{4.1}$$

to the time-averaged profiles of circumferential velocity taken along the z-axis. By assuming that the wandering vortex position has a bi-normal joint probability distribution function with specified values of the standard deviations ('wandering amplitudes') σ_y and σ_z in the y- and z-directions, Devenport *et al.* observed that the coefficients c_i and D_i could be corrected analytically using assumed values for σ_y and σ_z. Comparison is then made between the measured variances of the velocity fluctuations in the y- and z-directions at $(y, z) = (0, 0)$ and the estimated variances due to wandering of the corrected profile with amplitudes σ_y and σ_z under the assumption that turbulence within the core is negligible in comparison to velocity fluctuations due to wandering. If significant differences are detected, the wandering amplitudes are adjusted and the process is repeated until convergence is achieved.

The time-averaged radial profiles of circumferential velocity, fitted by equation (4.1), are shown in figure 4, together with the corresponding corrected profiles, for the no-grid, small-grid and large-grid cases at $X/c = 3.75$, 5.75, 7.75 and 9.75. For the no-grid case, the effect of wandering was essentially negligible, with very little

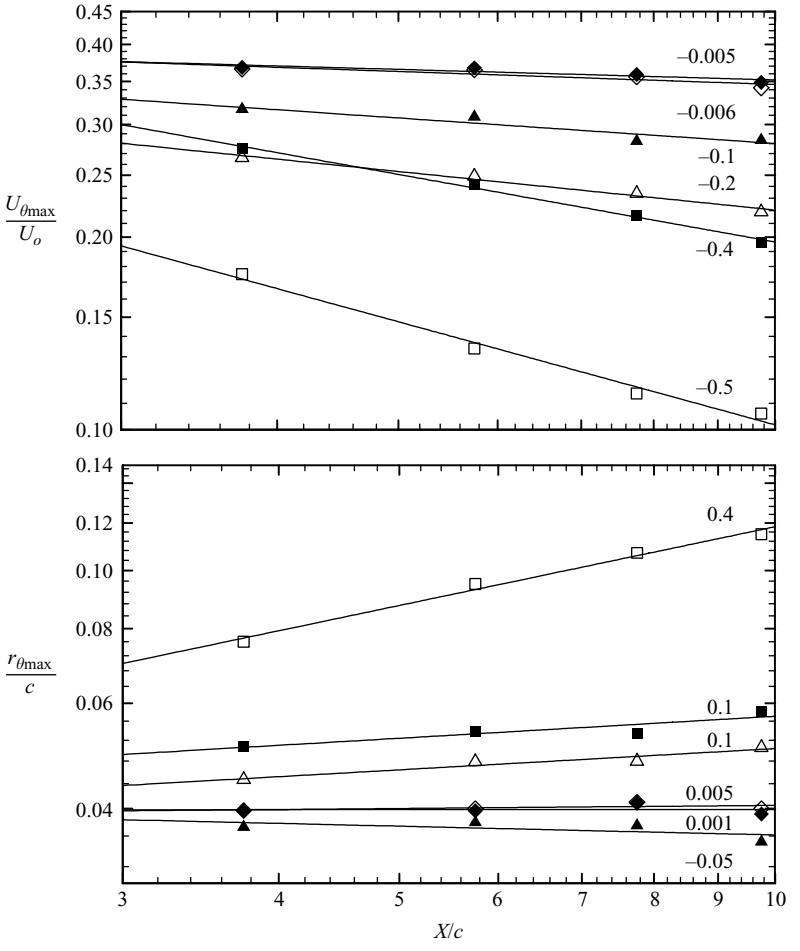

FIGURE 5. Streamwise developments of $U_{\theta\,\max}/U_o$ and $r_{\theta\,\max}/c$ for time-averaged (hollow symbols) and corrected (solid symbols) radial profiles for the no-grid (◇), small-grid (△) and large-grid (□) cases. Solid lines indicate power-law fits, with the exponent values indicated next to the lines.

development of the velocity profile in the streamwise direction. The small-grid and large-grid cases both indicated significant wandering as well as measurable decrease of the circumferential velocity with increasing streamwise distance.

For a quantitative description of wandering effects on the velocity profile, figure 5 shows the developments of the peak circumferential velocity $U_{\theta\,\max}$ and the radial location $r_{\theta\,\max}$ at which it occurs, for both the time-averaged and the corrected profiles. The no-grid case shows little change in $U_{\theta\,\max}$ and $r_{\theta\,\max}$ with streamwise distance. In contrast, $U_{\theta\,\max}$ decayed significantly for the small-grid case and, even more so, for the large-grid case. The corresponding changes of the corrected 'core size' $r_{\theta\,\max}$ were much slower. Power laws, indicated by solid lines in figure 5, were found to represent fairly well both the time-averaged (Bailey *et al.* 2006) and the corrected results.

As shown in figure 6, the wandering amplitudes σ_y and σ_z, determined using Devenport *et al.*'s procedure, were found to grow with streamwise distance for all cases and to increase with increasing free-stream turbulence. The amplitudes for the no-grid case remained lower than $0.006c$ (1 mm).

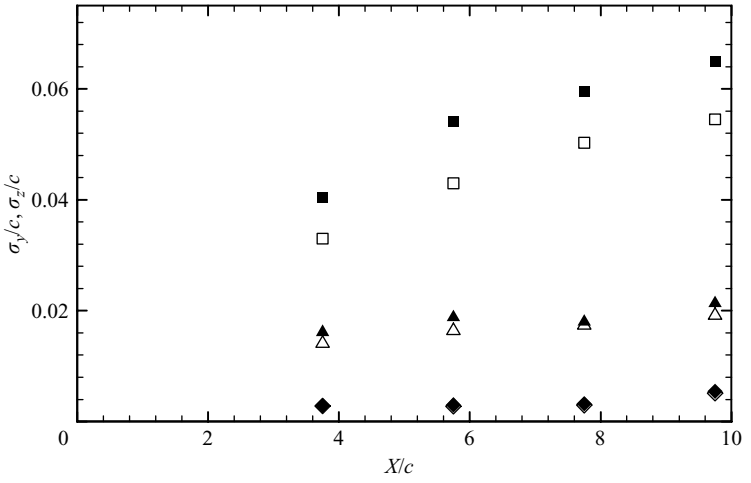

FIGURE 6. Wandering amplitudes σ_y (solid symbols) and σ_z (hollow symbols) for the no-grid ($\diamond$), small-grid ($\triangle$) and large-grid ($\square$) cases, estimated using the method of Devenport *et al.* (1996).

Although Devenport *et al.*'s correction technique applies well to low-turbulence cases, there are concerns about its application to high-turbulence ones. It was found that, as the wandering amplitude increased, the technique became increasingly sensitive to the number n of coefficients in the series fit. Small values of n resulted in poor fits, whereas large values of n achieved better fits, but also provided corrected profiles which were oscillatory and resulted in unrealistically large values of $U_{\theta\,\max}/U_o$, comparable to 1. For the turbulent free-stream cases, even small scatter in the time-averaged velocity profile introduced large oscillations in the corrected profile. Moreover, as the assumed wandering amplitude iterated to large amplitudes for the large-grid cases, the minimum realizable value of c_1 exceeded $r_{\theta\,\max}$, thus introducing an ambiguity in the local value of the velocity gradient, which, in turn, contaminated the determination of the peak location. Additional uncertainty in Devenport *et al.*'s correction technique would be introduced by turbulence within the vortex core, as might occur in the strong free-stream turbulence cases under consideration. This would generally result in over-correction of the profiles. Finally, this correction may also include errors introduced by the assumption of a bi-normal probability distribution of vortex position (Spalart 1998). These statements justify the need for estimating wandering effects using an improved statistical method. Such a method is described in the next subsection and applied to the reconstruction of the vortex velocity field from two-point measurements in § 5.

4.2. *Zero-crossing technique*

Consider a laminar vortex with its axis intersecting the measuring plane at position (y_v, z_v) and a probe located at position (y_p, z_p) and measuring velocity components U_{yv} and U_{zv} on this plane, as shown in figure 7. Instances at which the measurement volume passes through the axis of the vortex ($y_v = y_p$ and $z_v = z_p$) can be identified by the condition $U_{yv} = U_{zv} = 0$. In principle, one may use the relative frequencies of simultaneous zero crossings for U_y and U_z for different positions of the probe on a fixed streamwise plane to estimate the joint probability distribution function (j.p.d.f.) of (y_v, z_v). The standard deviations of the j.p.d.f. in different directions could then serve as measures of the vortex wandering amplitude. In practice, however, this approach has

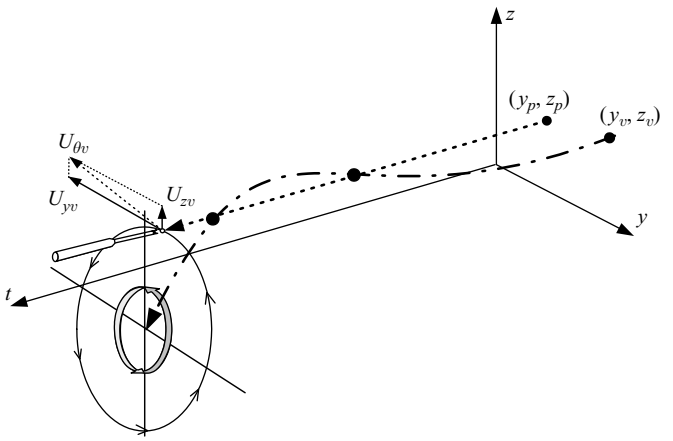

FIGURE 7. Sketch defining vortex position (y_v, z_v) in the (y, z)-plane, probe position (y_p, z_p) in the (y, z)-plane and the velocity components U_{yv}, U_{zv} induced by the vortex at the probe position as the vortex wanders in time.

two complications. First, the probe measures velocity with respect to the laboratory frame, whereas the interest is in velocity with respect to a frame attached to the wandering axis. This effect would be negligible if the transverse velocity of the vortex axis were very small compared to the local induced velocity. Second, turbulence in the vortex core, if appreciable, may introduce velocity zero crossings at locations different from the vortex axis. In the following, we will attempt to estimate the uncertainty in the determination of the vortex axis location caused by these two effects.

It seems reasonable to assume that, in a strongly turbulent free stream, the wandering of the vortex would be largely attributed to convection by the free-stream eddies. As the vortex resists deformation, its wandering velocity would probably be significantly lower than the local transverse velocity fluctuation in the free stream (in the absence of the vortex). Therefore, the amplitude of free-stream fluctuations may be considered as an upper bound for the amplitude of wandering velocity. For the purposes of estimating uncertainty, we consider as upper bound the value $2u'_y$, which is larger in magnitude than the free-stream fluctuations 95 % of the time. The amplitude of turbulent fluctuations in the vortex core is even harder to estimate. It is known that internal turbulence production within the vortex core is small (Devenport *et al.* 1996), and that the stabilizing effects of rotation would tend to eliminate turbulence within the vortex (Marshall & Beninati 2000). On the other hand, it is possible that the 'beating about' of the vortex by the free-stream turbulence and induction by nearby turbulent eddies might result in velocity fluctuations in the core, which may make a contribution to the local velocity measurement before they are eliminated by rotation. Again, it seems that a reasonable estimate of the upper bound of such motions would be $2u'_y$. Assuming that the two effects are statistically independent, one may estimate a likely upper bound of $2.8u'_y$ for interfering velocity fluctuations.

As an illustration of the uncertainty evaluation process, consider the large-grid case at $X/c = 9.75$, for which the free stream had $u'_y \approx 0.025U_o$. Then, the upper bound of the velocity fluctuation uncertainty would be $2.8u'_y \approx 0.07U_o$. Assuming that the radial gradients of circumferential velocity in the vortex core for the turbulent free-stream cases are not very different from that of the profile resulting from Devenport *et al.*'s correction, one may estimate the radial gradient of the circumferential velocity near

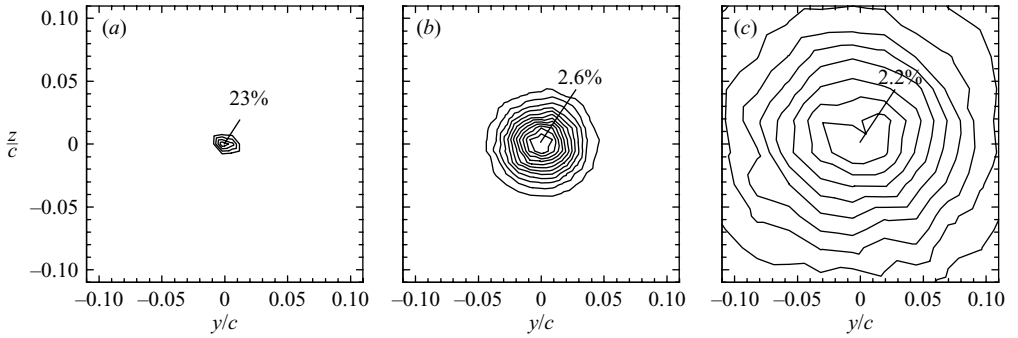

FIGURE 8. Isocontours of zero-crossing counts as a percentage of time-series length for the (*a*) no-grid, (*b*) small-grid and (*c*) large-grid cases ($X/c = 9.75$). Contour spacing is 5 % for the no-grid case and 0.2 % for the small-grid and large-grid cases.

the axis as $\partial U_\theta/\partial r \approx 0.03\, U_o\,\mathrm{mm}^{-1}$ (see figure 4, as an example). Then, one could infer that the previously estimated velocity uncertainty would introduce an uncertainty in the determination of the vortex axis location equal to $2.8u'_y/(\partial U_\theta/\partial r) \approx 2.1$ mm. This uncertainty is approximately 20 % of the estimated amplitude of the wandering motion, to be presented in following sections. Because this estimate represents an upper bound, the actual uncertainty is expected to be significantly smaller.

A different problem in this axis determination process arises when the probe is far away from the vortex axis, in essentially grid-generated turbulence. Then, U_θ would be of the order of u'_y and zero crossings that are unrelated to the passage of the vortex axis would be encountered. To remove a part of the turbulent fluctuations from the measured time series, while leaving wandering contributions unaffected, the time series were first digitally low-pass filtered before the zero-crossing count was conducted. The filter used was a double-pass fifth-order Butterworth filter with a cutoff frequency of 500 Hz, which was selected by visual inspection of the filtered time series. Note that this cutoff frequency limited the wavelengths of wandering captured by the analysis to those larger than $0.02c$, approximately equal to twice the largest integral scale of the turbulence. Comparison of the results with and without the filter indicated that the filter effectively removed false indications far from the time-averaged vortex axis; it is believed that the amplitude of the smaller wavelength motions did not make a significant contribution to the net amplitude of vortex wandering. Moreover, the probability that a zero crossing represented vortex axis passage and not free-stream turbulence was increased significantly by applying a condition on the streamwise velocity U_x. In general, $\overline{U}_x < U_o$ within the core (Bailey *et al.* 2006); for example, in the no-grid case at $X/c = 9.75$, for which the effect of wandering on the profile within the core is negligible, $U_x < 0.98U_o$ for $r/c < 0.08$. The additional condition for accepting a zero-crossing as representing passage of the vortex axis past the probe was set by trial and error as $U_x < 0.97U_o$. This threshold value was sufficiently high not to reject an excessive number of axis passages (which would make the statistics vulnerable to outliers) and sufficiently low to exclude the majority of zero crossings in grid turbulence.

Finally, allowance was made for the size of the probe by defining a zero crossing by the conditions $|U_y|, |U_z| \leqslant 0.05U_o$, rather than demanding exactness. These conditions identified instances at which the vortex axis was likely to be within the probe measurement volume, having a width of 0.5 mm.

As an example of this analysis, isocontours of zero crossings are presented for the no-grid (figure 8*a*), small-grid (figure 8*b*) and large-grid (figure 8*c*) cases at $X/c = 9.75$.

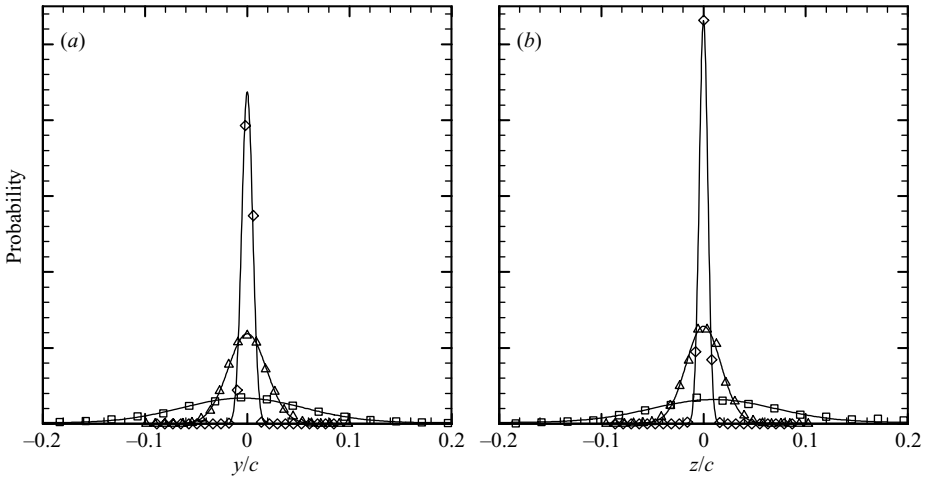

FIGURE 9. Probability density functions of vortex axis position relative to its time average in the (*a*) *y*- and (*b*) *z*-directions at $X/c = 9.75$ for the no-grid (◇), small-grid (△) and large-grid (□) cases.

Probability density functions of the instantaneous vortex axis position along the *y*- and *z*-axes, estimated from zero crossings within ranges of $\pm 0.01c$ along each axis, are presented in figure 9. In all cases, the time-averaged vortex axis position has the maximum probability of being also the instantaneous axis position. The same figure also illustrates a dramatic strengthening of axis wandering with increasing free-stream turbulence. Gaussian curves described the measurements in all directions. This observation extends Devenport *et al.* (1996)'s normality hypothesis for vortex wandering in low-turbulence free streams to the case of free streams with isotropic turbulence. The wandering amplitude for each measurement case can be confidently represented by the standard deviation σ of the distance between the instantaneous and time-averaged vortex axis positions, as determined by the zero-crossing method, and conveniently estimated from the fitted Gaussian curves. To illustrate the soundness of this approach, it is noted that the measurements for the no-grid case at $X/c = 9.75$ gave $\sigma \approx 0.8$ mm, which was not far from the estimate of 1 mm, using Devenport *et al.*'s technique. It may be noted that the difference between these two values is within the expected uncertainties of the zero-crossing technique and the probe positioning system and comparable to the spatial resolution of the hot-wire probe.

To quantify the effect of conditioning on the zero-crossing population, consider the results for the large-grid case at $X/c = 9.75$. Far away from the core, at $y = z = -0.15c$, where the zero crossings are predominantly expected to be caused by turbulent fluctuations and zero crossings occurred 9.0 % of the time, filtering was found to decrease the accepted zero crossings by 1.5 % of all velocity samples, whereas the condition $U_x < 0.97U_o$ further decreased them by an additional 7.5 %. In contrast, on the time-averaged vortex axis, where zero crossings occurred 2.8 % of the time, filtering and the $U_x < 0.97U_o$ condition decreased the number of accepted zero crossings by less than 0.1 % and by about 0.5 %, respectively.

The dependence of the estimated wandering amplitudes on streamwise distance is presented for three cases in figure 10. In this figure, σ_y and σ_z were estimated from fitted Gaussian curves to p.d.f.s along the *y*- and *z*-axes, respectively.

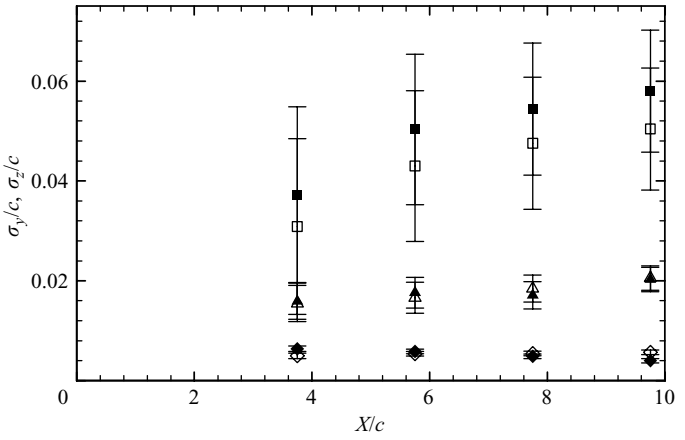

FIGURE 10. Estimated wandering amplitude in y (solid symbols) and z (hollow symbols) directions using simultaneous zero-crossings for the no-grid ($\diamond$), small-grid ($\triangle$) and large-grid ($\square$) cases. Error bars represent estimated uncertainty in identifying the instances when the probe and vortex centre are coincident due to internal turbulence and convective velocity of the vortex.

The confidence in the wandering-amplitude estimates can be tested by comparing values calculated using the technique of Devenport *et al.* (1996) and those obtained independently by using the zero-crossing technique. For the small-grid case, the former technique gave $\sigma_y = 2.9$, 3.3, 3.2 and 3.8 mm, respectively, for $X/c = 3.75$, 5.75, 7.75 and 9.75, whereas the corresponding values from the latter technique were 2.8, 3.1, 3.0 and 3.6 mm. Differences between these values are well within the expected uncertainty and increase the confidence in these estimates. For the large-grid case, such differences were somewhat larger, although still not excessive: Devenport *et al.* (1996)'s technique gave $\sigma_y = 7.2$, 9.6, 10.6 and 11.5 mm at the corresponding X/c location, whereas zero crossing count gave $\sigma_y = 6.6$, 8.9, 9.6 and 10.3 mm. The differences between corresponding estimates increased with increasing streamwise distance, which reflects the increasing uncertainty in Devenport *et al.*'s technique at higher wandering amplitudes and the increased errors discussed above for the zero-crossing technique. Figures 6 and 10 also illustrate some small differences between σ_y and σ_z, which were strongest for the large-grid case, in which $\sigma_y/\sigma_z \approx 1.2$ for all X/c examined.

4.3. *Frequency analysis of vortex motion*

Temporal characteristics of the vortex wandering were examined using frequency spectra $F_{yy}(f)$ of U_y on the time-averaged vortex axis, where the contribution of wandering to the total fluctuation energy is the greatest. Sample spectra, measured at $(y, z) = (0, 0)$ for the no-grid, small-grid and large-grid cases at $X/c = 3.75$, 5.75, 7.75 and 9.75, are shown in figure 11. Note that, in general, the frequency spectra of U_y and U_z were comparable on and near the time-averaged vortex axis, but their differences increased with increasing distance from the axis. A peak at 30 Hz can be discerned for the no-grid case, but this peak is associated with vibration of the probe due to wind-tunnel vibrations, as explained by Bailey (2006).

Power spectra in this flow contain contributions from several sources, including vortex wandering, free-stream turbulence, turbulence originating in the spiral wake and possible instabilities within the vortex core. It is expected that contributions of

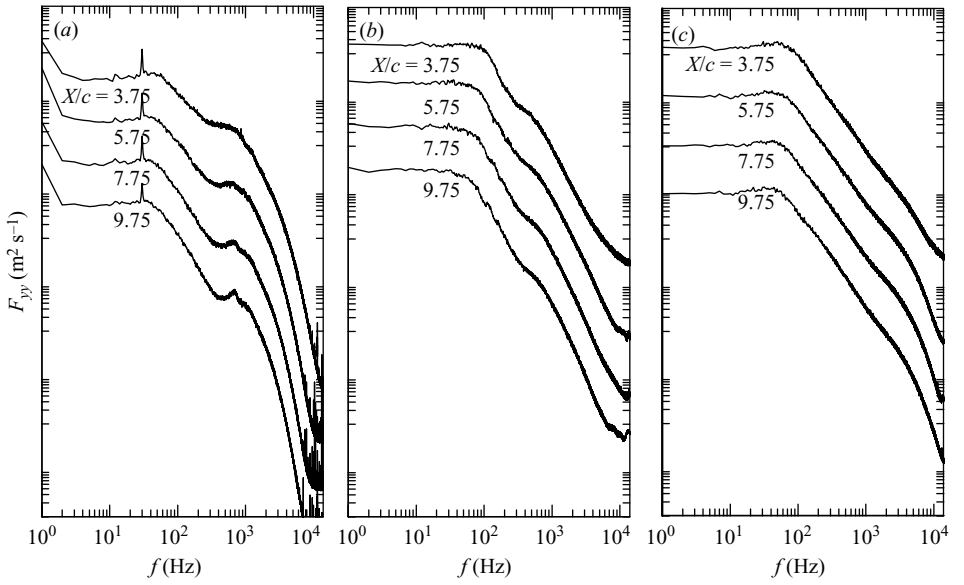

FIGURE 11. Frequency spectra of U_y on the time-averaged axis for the (*a*) no-grid, (*b*) small-grid and (*c*) large-grid cases. Except for the ones at $X/c = 3.75$, the spectra have been shifted down by one, two or three decades to prevent clutter. Scales are arbitrary but the same for the three sets of plots.

wandering motions would appear at significantly lower frequencies than those of turbulent activities. Additional complications arise because wandering acts as spatial averaging of the spectra, as the probe measures energy contributions from a range of locations in the flow. Consequently, it is possible that some measured spectra could express several distinct patterns at once that dominate the vortex core, the spiral wake or the free stream. Vortex wandering effects are expected to be prevalent in spectra measured in the vortex core.

As shown in figure 11, the frequency spectra on the time-averaged axis have a significantly different appearance for the three cases considered. The no-grid case (figure 11*a*) has its highest energy level at $f < 1$ Hz, followed by a plateau in the range $1 < f < 100$ Hz. For $100 < f < 400$ Hz, these spectra show a roll-off with constant slope, followed by another plateau containing a possible peak in the range $400 < f < 1000$ Hz. At $f > 1$ kHz, the energy decreases at a continuously increasing rate. A spike of energy is observed at about 700 Hz, the amplitude of which is found to grow with increasing streamwise distance. This spike, believed to be associated with an instability in the vortex core and evident for the no-grid case only, was in agreement with observations by Singh & Uberoi (1976) and Bandyopadhyay *et al.* (1991). This instability was not investigated in depth, as it was deemed to be outside the scope of the present work. Frequency spectra for the small-grid case show a relatively flat region for $f \lesssim 100$ Hz, followed by a roll-off of constant slope in the range $100 \lesssim f \lesssim 300$ Hz. At $f \approx 300$ Hz, there is a 'kink' in the spectra, followed by a roll-off of increasing slope with increasing frequency. Frequency spectra for the large-grid case appear generally similar to those in the small-grid case, but exhibit only a barely visible kink at $f \approx 1.2$ kHz. Also evident in the large-grid case, but not in the small-grid case, is a broadband peak, centred at $f \approx 40$ Hz.

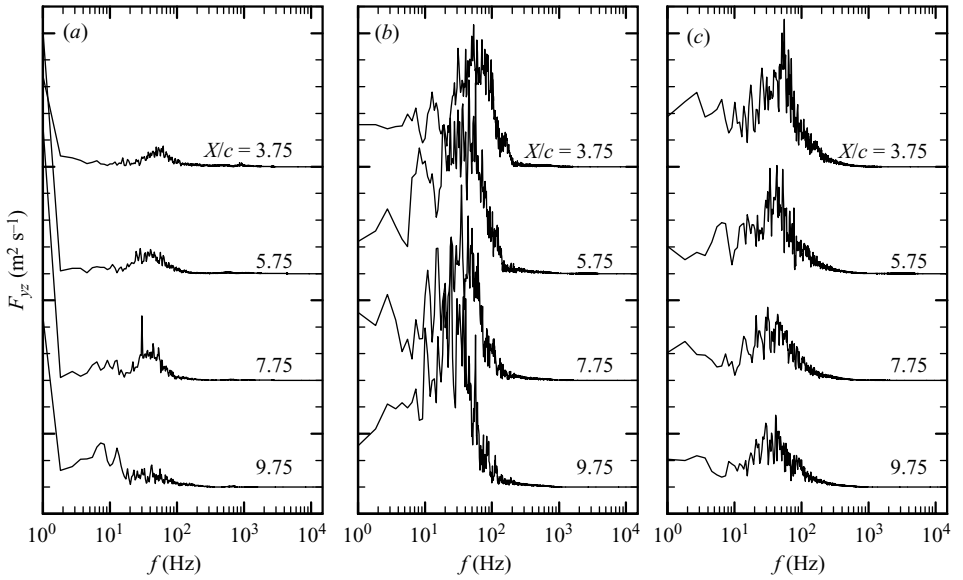

FIGURE 12. Cross-spectra of U_y and U_z on the time-averaged vortex axis for the (*a*) no-grid, (*b*) small-grid and (*c*) large-grid cases. Axes are semi-logarithmic, and spectra at successive streamwise locations have been shifted downwards for clarity.

Comparing the spectra in the three cases, one may readily observe that they all display a plateau in the low-frequency range ($f \lesssim 100$ Hz), followed by a roll-off of constant slope up to some frequency where there is a kink in the spectra. It is believed that these features are the signature of vortex wandering.

In order to investigate the possible connection between the broadband peak observed for the large-grid case and the dominant wavelengths of vortex wandering, cross-spectra F_{yz} of U_y and U_z were measured and their magnitudes are shown in figure 12 in semi-log plots. Because wandering affects both components of velocity simultaneously, the cross-spectra are expected to show more prominently the frequency range of wandering than power spectra would. This figure indicates the presence of broadband peaks at f_p, whose exact locations were identified by fitting the spectra in the range between 30 and 50 Hz with 40th-order polynomials in terms of $\log(f)$. An estimate of the characteristic wavelength of vortex wandering can be obtained as U_o/f_p. The streamwise development of this parameter is shown in figure 13. The dimensionless wavelengths $U_o/f_p c$ were comparable in all three cases, initially growing between $X/c = 3.75$ and 5.75, but then remaining nearly constant further downstream. It is also interesting to note that U_o/f_p is an order of magnitude larger than the longitudinal integral length scale of the free-stream grid turbulence measured without the wing. Moreover, U_o/f_p was found to be one to two orders of magnitude greater than the wandering amplitude (figure 10).

Also evident for the no-grid case (figure 12*a*) is a peak at a frequency near 7 Hz. This peak increases in amplitude with streamwise distance, such that, at $X/c = 9.75$, it contains more energy than the peak between 30 and 50 Hz. Also evident is a significant amount of energy for $f \lesssim 2$ Hz. These observations seem to indicate that for the no-grid case there are multiple sources of the wandering, each of which may have a different range of dominant frequencies. Although these sources may also be

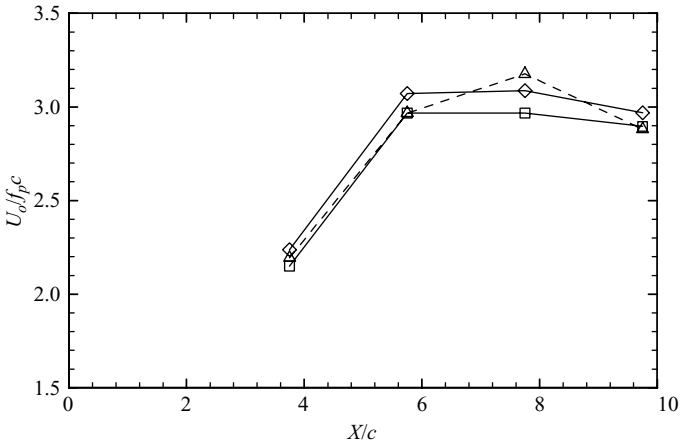

FIGURE 13. Wavelength of wandering for the no-grid (◇), small-grid (△) and large-grid (□) cases, identified from cross-spectra of U_y and U_z at $(y, z) = (0, 0)$.

present in the grid-turbulence cases, their effects are less visible in the spectra, which appear to be dominated by a single main source of wandering.

5. Reconstruction of velocity profiles in the wandering frame

5.1. *Procedure*

The vortex wandering analysis has demonstrated that, as the free-stream turbulence increases, so too does the amplitude of vortex wandering. When wandering becomes intense, time-averaged profiles of the velocity and other properties measured by a fixed probe would deviate significantly from corresponding properties of the vortex that would be measured by a probe following the vortex axis in its motion. The objective of this section is to reconstruct radial profiles of vortex properties in a frame of reference that is attached to the wandering vortex axis using two four-sensor hot-wire probes.

To determine the velocity at a given radial position with respect to the instantaneous vortex axis, $\tilde{r}$, the measurements of each probe were sorted upon a condition applied to the measurements of the other probe. The challenge in this procedure was to identify the locations of the two probes relative to the vortex axis. The first step was to determine instances at which the vortex axis intersected the line joining the two probe measurement volumes. In a laminar vortex, such instances would be identified by either of the conditions $U_{y1} \approx 0$ or $U_{y2} \approx 0$, because the probes are separated along the y-axis (see figure 14; subscripts 1 and 2 indicate measurements by probes 1 and 2, respectively, and the subscripted v indicates the velocity induced by the vortex). However, in a turbulent vortex, non-zero radial velocity could be measured by one probe when the other one reads a zero radial component. Differences between reconstructed velocity profiles obtained by applying the stricter condition $U_{y1} \approx U_{y2} \approx 0$ and those obtained using the simplified condition $U_{y1} \approx 0$ were found to be not significant, although the latter were slightly smoother owing to the larger accepted data populations. In this process, the threshold below which a transverse velocity magnitude was considered to be negligible was set at $0.03U_o$, which corresponds to an estimated uncertainty of 0.3 mm in locating the vortex axis in the no-grid case. For the measurements passing this condition, the instantaneous

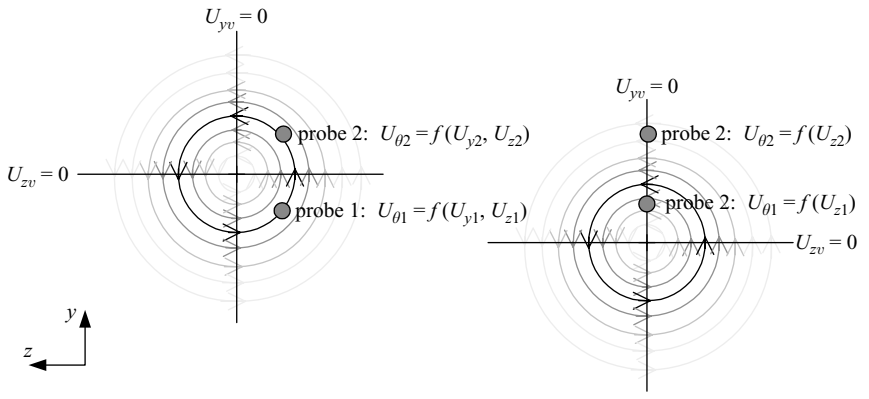

FIGURE 14. Sketch illustrating the relationship between velocity components U_{yv} and U_{zv} induced by the vortex and the velocity components measured by the two probes. When U_{y1} or $U_{y2} = 0$, $U_{z1} = U_{\theta 1}$ and $U_{z2} = U_{\theta 2}$.

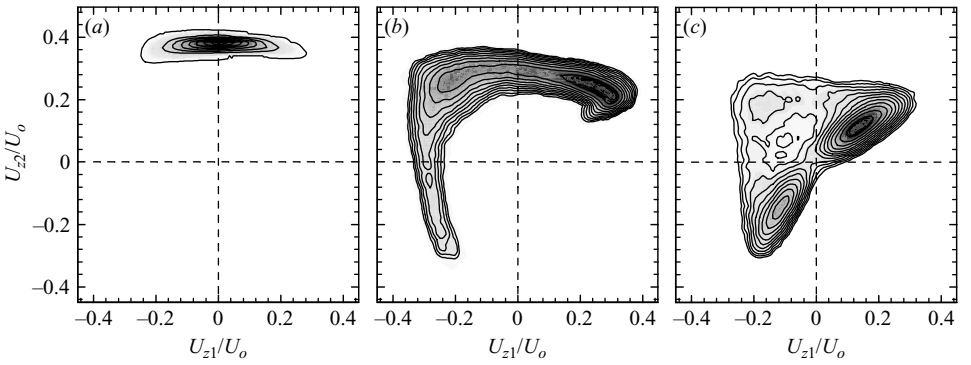

FIGURE 15. Joint probability density functions of U_{z1} and U_{z2} conditioned on $U_{y1} \approx 0$ for the (*a*) no-grid, (*b*) small-grid and (*c*) large-grid cases at $X/c = 9.75$ and with $S = 7.1$ mm. Contour lines are spaced at intervals increasing exponentially to highlight features at low probability. Darker shading indicates higher probability.

circumferential velocity in the vortex was determined by setting $U_{\theta 1} \approx |U_{z1}|$ and $U_{\theta 2} \approx |U_{z2}|$ (see figure 14).

The next step in the analysis was to determine the radial locations of the two probes for each of the instances satisfying the above condition. To do this, the conditional j.p.d.f. of U_{z1} and U_{z2}, conditioned on $U_{y1} \approx 0$, was utilized. Figure 15 shows examples of such j.p.d.f. for the no-grid, small-grid and large-grid cases at $X/c = 9.75$ with $S = 7.1$ mm. Isocontours of the j.p.d.f.s follow a distinct pattern, which is dictated by the velocity induced by the vortex at different positions with respect to the probe locations. Different regions of this pattern identify distinct regimes of the instantaneous locations of the probes with respect to the vortex axis, as illustrated in figure 16(*a*). The full pattern is not evident in the no-grid j.p.d.f., because the wandering amplitude was too small for probe 1 to travel outside the vortex core. As the wandering amplitude increased, however, the probes measured velocities at increasingly larger distances from the instantaneous vortex axis and hence the pattern became evident for the small-grid case and even more pronounced for the large-grid

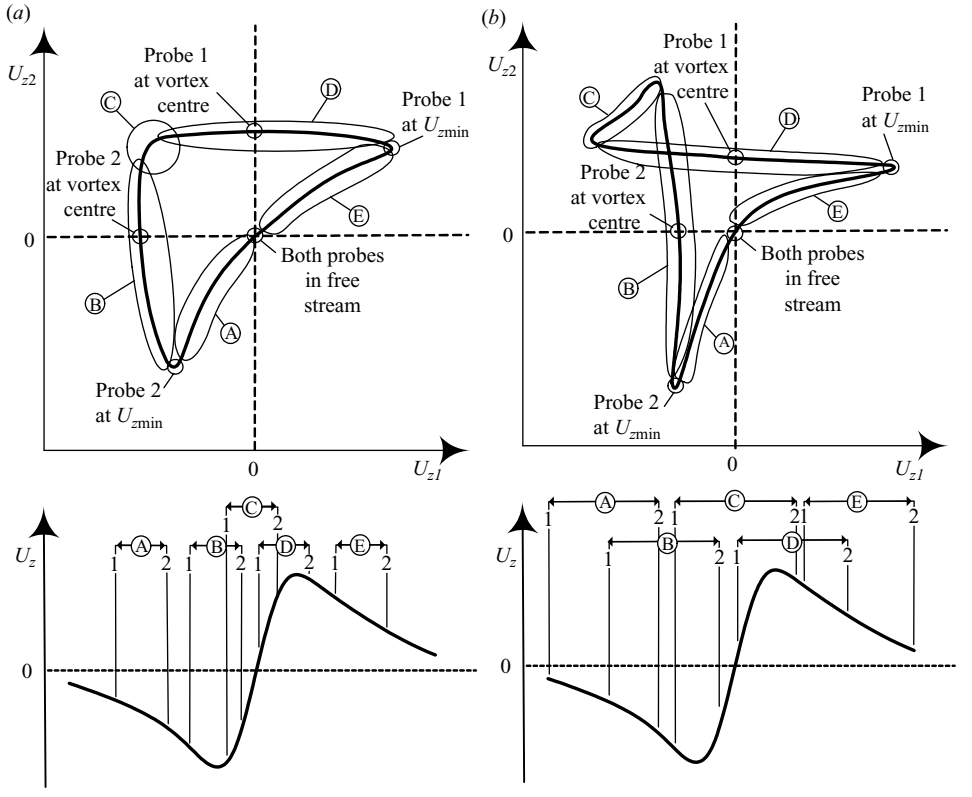

FIGURE 16. Sketch illustrating locations of different regimes on the j.p.d.f. of U_{z1} and U_{z2} conditioned for $U_{y1} \approx 0$ for (*a*) small and (*b*) large values of S.

case, for which the wandering amplitude was sufficiently large for the entire vortex to have wandered past both probes.

As probe spacing increased, the pattern of the j.p.d.f. isocontours started to deviate from that shown in figure 16(*a*), reflecting a decreasing probability of the combined event that both probes would be within the vortex core at the same time. In addition, a new regime became more evident, corresponding to the event that the two probes were on opposite sides of the core. Hence, the pattern of isocontours depends on the relative size of probe spacing compared to the vortex core radius.

Examples of j.p.d.f. isocontours for $S = 19.6$ mm are shown in figure 17 for the no-grid, small-grid and large-grid cases at $X/c = 9.75$. As with figure 15, a distinct pattern is evident; however, the pattern of the j.p.d.f. contours is slightly different from the one shown in figure 16(*a*). Even so, different regimes can still be identified, as illustrated in figure 16(*b*). Thus, there is discernible relationship between the simultaneous velocity measured by the two probes and their relative position in the vortex. In particular, the instance when probe 1 is on the vortex axis can be readily identified by the condition of $U_{z1} = 0$, allowing determination of the corresponding velocity at $U_{z2}(S)$.

5.2. *Outer profile reconstruction*

The outer portions of the radial profiles ($7.1 < \tilde{r} < 27.6$ mm) of the circumferential velocity were reconstructed as follows. First, instances at which $U_{y1} \approx U_{z1} \approx 0$ were identified. These instances occurred when the axis of the vortex passed through probe 1 and correspond to the line $U_{z1} = 0$ on the j.p.d.f. of U_{z1} and U_{z2} with the condition

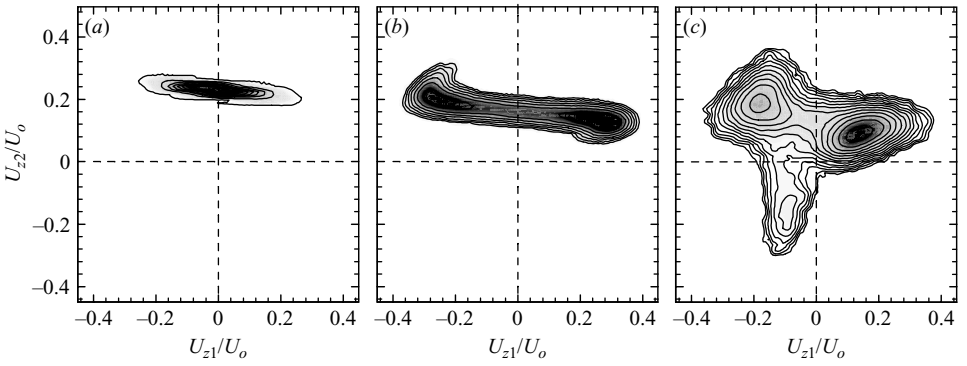

FIGURE 17. Joint probability density functions of U_{z1} and U_{z2} conditioned on $U_{y1} \approx 0$ for the (*a*) no-grid, (*b*) small-grid and (*c*) large-grid cases at $X/c = 9.75$ and with $S = 19.6$ mm. Contour lines are exponentially distributed to highlight features at low probability. Darker shading indicates higher probability.

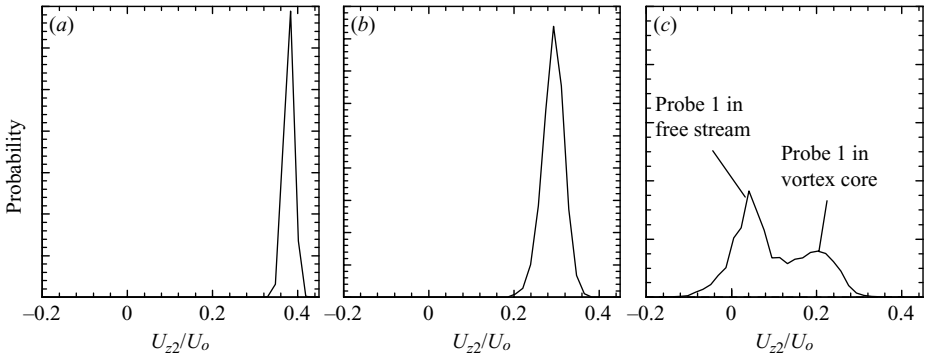

FIGURE 18. Cross-sections at $U_{z1} = 0$ of j.p.d.f. measured at $X/c = 9.75$ and $S = 7.1$ mm for (*a*) no-grid, (*b*) small-grid and (*c*) large-grid cases.

$U_{y1} \approx 0$ (indicated by vertical dashed lines in figures 15 and 17). In other words, the values of U_{z2} along the line $U_{z1} = 0$ are values measured by probe 2 when probe 1 is on the instantaneous vortex axis. Thus, the cross-section of the j.p.d.f. along this line may be taken to approximately represent the p.d.f. of the circumferential velocity at a radial distance from the instantaneous vortex axis that is equal to the probe spacing. The average value of U_{z2}, determined from the p.d.f., should therefore be $\widetilde{U}_\theta(\widetilde{r} = S)$, where tildes indicate average values in the wandering frame. Such cross-sections of the j.p.d.f. shown in figure 15 are plotted in figure 18. For the no-grid and small-grid cases, the p.d.f.s were nearly Gaussian, whereas for the large-grid case, the p.d.f. was double-peaked. Note that, in view of the large wandering amplitude for the large-grid case, and the relatively high probability of instances when probe 1 and probe 2 were both in the free stream and subjected to velocity fluctuations in the free-stream turbulence (compare figure 15*c* to figure 16), averaging the p.d.f. results would result in inaccurate estimates of $\widetilde{U}_\theta$. Therefore, for the large-grid case alone, the U_{z2} value at the appropriate p.d.f. peak (see figure 18) was used as estimate of $\widetilde{U}_\theta$.

By determining $\widetilde{U}_\theta$ for different values of S, the average radial profile of the vortex circumferential velocity, relative to the vortex axis, was reconstructed for the range $7.1 \leqslant \widetilde{r} \leqslant 27.6$ mm. As an example of the reconstruction, the portions of the radial

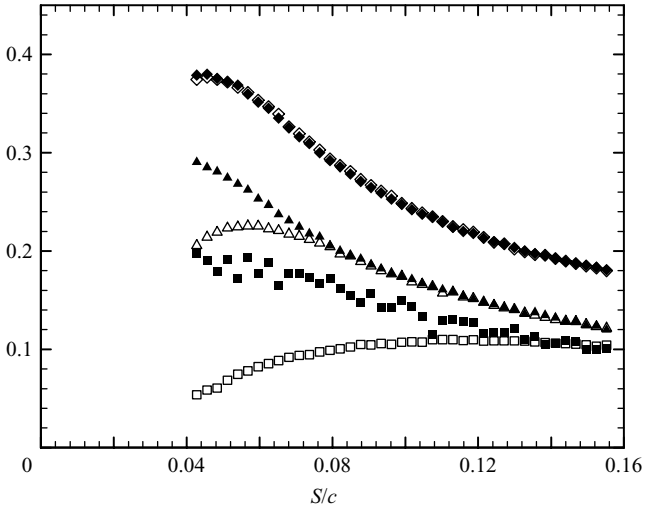

FIGURE 19. Comparison of $\widetilde{U}_\theta(S)$ (solid symbols) to $\overline{U}_{z2}(S)$ (hollow symbols) in the range $7.1 \leqslant S \leqslant 27.6$ mm for the no-grid ($\diamond$), small-grid ($\triangle$) and large-grid ($\square$) cases at $X/c = 9.75$.

profiles determined using this technique for the no-grid, small-grid and large-grid cases at $X/c = 9.75$ are indicated by solid symbols in figure 19. Also indicated in figure 19 by open symbols are the corresponding time-averaged profiles $\overline{U}_{z2}(S)$. The noticeably increased scatter in the large-grid case reflects the relatively small population of instances at which probe 1 coincided with the vortex axis.

5.3. *Inner profile reconstruction*

Because the probe separation could not be reduced below 7.1 mm, the method described in the previous subsection could not be used to reconstruct the velocity profile in the inner vortex core ($\widetilde{r}/c < 0.04$); instead, a more elaborate method was devised, as follows.

First, the j.p.d.f. of U_{z1} and U_{z2}, conditioned on $U_{y1} \approx 0$, was determined at some intermediate spacing, e.g. $S = 14.1$ mm. At this spacing, when probe 1 is in the vortex core, probe 2 is in a region where the velocity gradient is relatively large. Next, the most probable values of U_{z2} for 40 discrete values of $U_{z1} \geqslant 0$ were estimated as the values with peak probability in the corresponding j.p.d.f. cross-section (quadratic interpolation was used to locate the peaks); these most probable values are represented by the function $U_{z2} = f(U_{z1})$. Then, assuming that probe 2 was positioned outside the core, its most likely radial position was estimated by interpolating a fourth-order polynomial fitted to the outer portion of the reconstructed velocity profile, which was determined as described in the previous subsection; this radial position is represented as $\widetilde{r}_2 = g(U_{z2})$. Next, the most likely radial position $\widetilde{r}_1$ of probe 1, which included locations in the inner vortex core, was determined for each of the 40 discrete values of U_{z1}, as $\widetilde{r}_1 = g(f(U_{z1})) - S$. Finally, the reconstructed velocity profile in the inner core could be estimated as $\widetilde{U}_\theta(\widetilde{r}) = U_{z1}(\widetilde{r}_1)$.

Unfortunately, the applicability of this method was restricted to relatively small values of U_{z1}, because, as U_{z1} increased, it became increasingly difficult to distinguish whether probe 1 was within or outside the vortex core. In practice, the reconstruction of the inner profile was reliable and independent of the choice of probe separation used in the process for $U_{z1} < 0.25U_o$ for the no-grid case and $U_{z1} < 0.22U_o$ for the

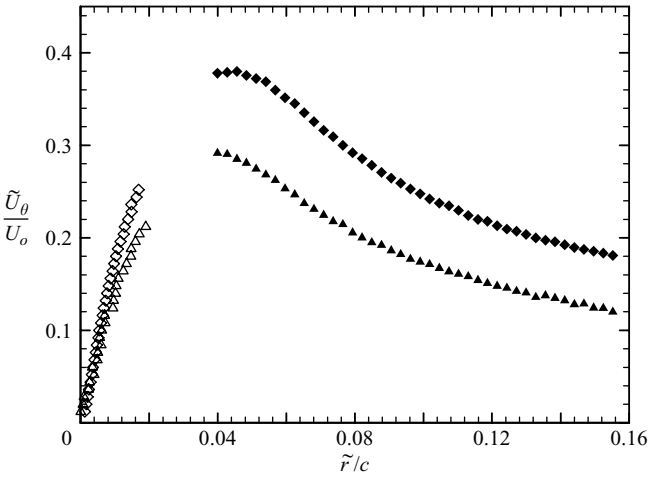

FIGURE 20. Inner profile reconstruction (hollow symbols) for the no-grid (◇) and small-grid (△) cases at $X/c = 9.75$. Corresponding reconstructed outer profiles are shown for comparison using solid symbols.

small-grid case. For the large-grid case, this method was deemed to be unreliable. Examples of reconstructed inner profiles are shown in figure 20.

5.4. *Reconstructing the missing parts of the vortex profiles*

The peak circumferential velocity $\widetilde{U}_{\theta\,\max}$ and its radial location $\widetilde{r}_{\theta\,\max}$ are important scales of the vortex evolution. Unfortunately, these scales cannot be determined with certainty from the previous methods, as it appears (figure 19) that $\widetilde{r}_{\theta\,\max}$ was slightly less than the minimum probe spacing. Therefore, it is necessary to reconstruct the full velocity profile. For the no-grid and small-grid cases, for which reconstructed inner portions of the profiles were available, the missing portions were estimated from interpolated radial profiles

$$\widetilde{\Gamma}(\widetilde{r}) = 2\pi r \widetilde{U}_\theta(\widetilde{r}) \tag{5.1}$$

of the circulation in a wandering frame, under the assumption that the vortex is axisymmetric. Interpolation was performed by fitting a fourth-order polynomial to the four nearest points of the outer and the four nearest points of the inner portions of the reconstructed profile. Inspection of typical reconstructed circulation profiles, shown in figure 21(*a*), demonstrates the obvious soundness of this approach. Then, the corresponding missing portions of $\widetilde{U}_\theta(\widetilde{r})$ were determined by inverting equation (5.1); such profiles are shown in figure 21(*b*).

The inner portion of the velocity profile for the large-grid case was reconstructed by assuming that the velocity profiles in the present experiments were self-similar and described by the following empirical expression (Phillips 1981):

$$\frac{U_\theta}{U_{\theta\,\max}} = \left[1.772\left(\frac{r}{r_{\theta\,\max}}\right)^2 - 1.0467\left(\frac{r}{r_{\theta\,\max}}\right)^4 + 0.2747\left(\frac{r}{r_{\theta\,\max}}\right)^6\right]\frac{r_{\theta\,\max}}{r}, \tag{5.2a}$$

for $r/r_{\theta\,\max} \leqslant 0.92$, and

$$\frac{U_\theta}{U_{\theta\,\max}} = \left[\ln\left(\frac{r}{r_{\theta\,\max}}\right) + 1\right]\frac{r_{\theta\,\max}}{r} \tag{5.2b}$$

for $0.92 \leqslant r/r_{\theta\,\max} \leqslant 1.2$.

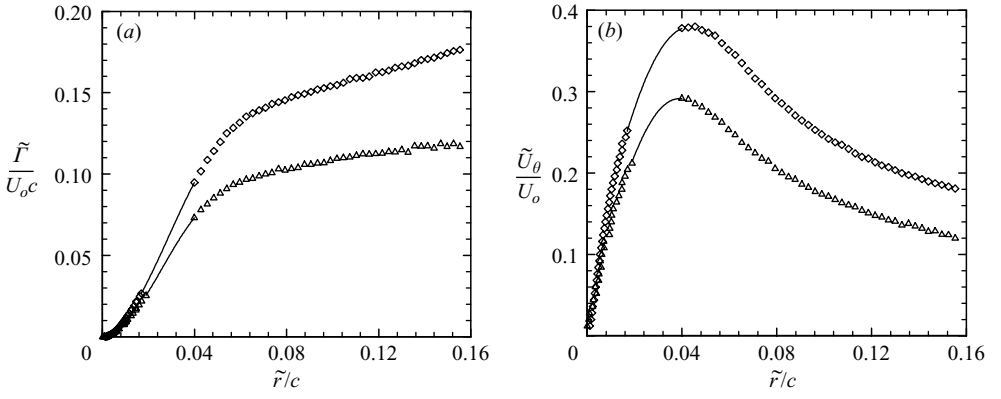

FIGURE 21. Curve fits (solid lines) used to connect the inner and outer portions of the reconstructed profiles of (*a*) $\widetilde{\Gamma}$ and (*b*) $\widetilde{U}_\theta$ for the no-grid (◇) and small-grid (□) cases at $X/c = 9.75$.

The reconstruction technique consists of first selecting appropriate values of $\widetilde{r}_{\theta\,\max}$ and $\widetilde{U}_{\theta\,\max}$ to match the reconstructed outer portion of the velocity profiles, and then extrapolating equation (5.2*b*) towards $\widetilde{r} = 0$. As described by Bailey (2006), it was found to be easier to match Phillips' expression to the experimental results by using $\widetilde{\Gamma}(\widetilde{r})$ to estimate $\widetilde{U}_{\theta\,\max}$ and $\widetilde{U}_\theta(\widetilde{r})$ to estimate $\widetilde{r}_{\theta\,\max}$ since $\widetilde{\Gamma}(\widetilde{r})$ was relatively insensitive to $\widetilde{r}_{\theta\,\max}$. The estimated uncertainties in $\widetilde{U}_{\theta\,\max}/U_o$ and $\widetilde{r}_{\theta\,\max}$ were 0.2 % and 0.3 mm, respectively.

Reconstructed velocity profiles are shown in figure 22. For the no-grid case, the reconstructed profiles essentially matched the time-averaged profiles and changed little downstream. The inflectional profile observed at $X/c = 3.75$ is not likely to be an artefact of the reconstruction technique; a similar profile was also observed at $X/c = 4.75$ by Devenport *et al.* (1996), who attributed it to persisting effects of the multiple vortices at the tip of the wing. The reconstructed profiles show good general agreement with corresponding time-averaged profiles, corrected using Devenport's method (figure 4). For the small-grid and large-grid cases, $\widetilde{U}_{\theta\,\max}$ visibly decreased with streamwise distance, whereas $\widetilde{r}_{\theta\,\max}$ did not show any obvious change.

The streamwise evolutions of $\widetilde{r}_{\theta\,\max}$ and $\widetilde{U}_{\theta\,\max}$ are shown in figure 23. Despite the appreciable uncertainty and scatter, it seems fair to conclude that there is no significant systematic dependence of $\widetilde{r}_{\theta\,\max}$ on either streamwise distance or free-stream turbulence level. In contrast, there is a noticeable decrease of $\widetilde{U}_{\theta\,\max}$ both with increasing streamwise distance and with increasing free-stream turbulence. Power laws of the type

$$\widetilde{U}_{\theta\,\max}/U_o = A(X/c - X_o/c)^{-n} \tag{5.3}$$

where the virtual origin $X_o = -0.25c$, with $A = 0.4$ for all cases and $n = 0.015$, 0.135 and 0.295 for the no-grid, small-grid and large-grid cases, respectively, could be fitted to the data.

5.5. *Effect of vortex bending*

The accuracy of the vortex velocity profile reconstruction could be affected adversely by a misalignment of the vortex axis and the normal direction to the measurement plane. Such misalignment would decrease the apparent azimuthal component of the velocity vector and increase the apparent cross-sectional area of the vortex core,

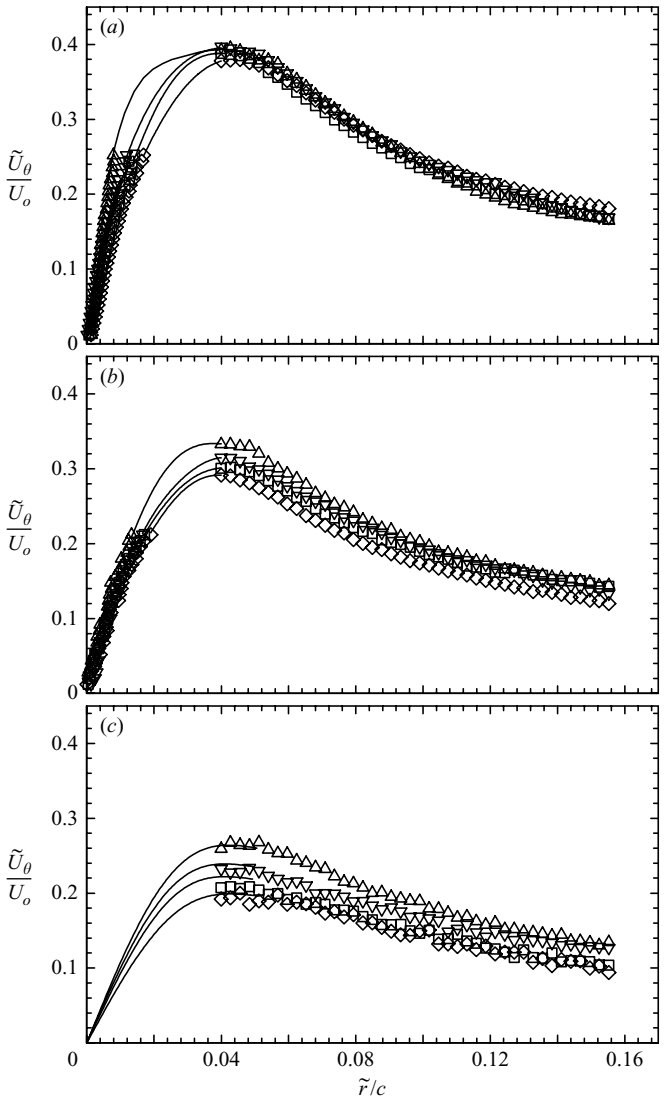

FIGURE 22. Radial profiles of $\widetilde{U}_\theta$ at $X/c = 3.75$ ($\triangle$), 5.75 ($\triangledown$), 7.75 ($\square$) and 9.75 ($\diamond$) for the (a) no-grid, (b) small-grid and (c) large-grid cases.

introducing an apparent diffusion of $\widetilde{U}_\theta(\widetilde{r})$. The angle between the vortex axis and the normal to the measurement plane can be measured by the ratio of the amplitude of vortex wandering and its wavelength. Vortex bending occurs over a range of wavelengths. Short-wavelength motions, such as those induced by azimuthally aligned secondary vortical structures, could, if sufficiently strong, reduce the accuracy of the reconstruction. However, the amplitude of such motions was estimated to be small relative to the large-scale meandering introduced by the isotropic free-stream eddies, which is the dominant mechanism causing vortex bending. A rough estimate of the average wavelength to amplitude ratio of this dominant motion can be determined by comparing the results of figures 13 and 10, which indicate that the dominant wandering wavelength U_o/f_p was almost two orders of magnitude greater than the

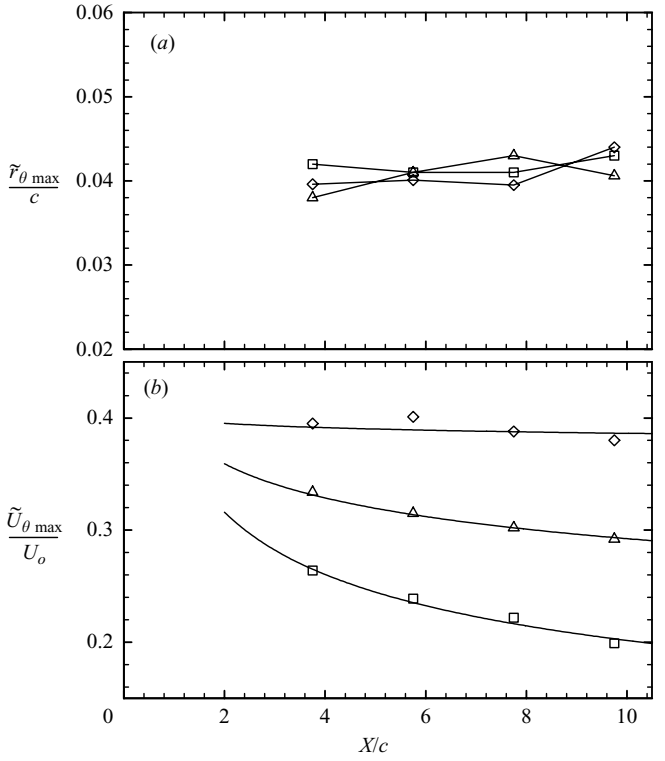

FIGURE 23. Streamwise development of (*a*) $\tilde{r}_{\theta\,\max}/c$ and (*b*) $\tilde{U}_{\theta\,\max}/U_o$ for no-grid (◇), small-grid (△) and large-grid (□) cases. Solid lines in (*b*) indicate power law fit of equation 5.3.

wandering amplitude σ. This corresponds to a typical misalignment angle of about 10° (Bailey 2006), which would have a negligible effect on the reconstruction of the average velocity profile in the wandering frame.

5.6. *Reverse estimates of time-averaged statistics*

To further test the accuracy of the reconstructed velocity profiles, they were used, in combination with the statistically specified wandering motion, to generate independent estimates of radial variations of time-averaged properties, which were then compared to corresponding measured variations. To do so, consider a laminar vortex with an axisymmetric velocity field, as reconstructed in previous subsections (figure 22), and wandering such that its transverse position is statistically described by the experimentally determined j.p.d.f. (figure 8). A simulated time series of vortex coordinates y_v and z_v on the transverse plane was constructed using a number generator, which generated normally distributed random numbers with standard deviations equal to measured values of σ_y and σ_z, respectively. Then, consider a position (y_p, z_p), representing the probe measuring volume. For each position of the 'vortex', the induced velocity components at the 'probe' position were determined as

$$U_{yv} = -\widetilde{U}_\theta(r_p)\sin(\theta_p) \tag{5.4}$$

and

$$U_{zv} = \widetilde{U}_\theta(r_p)\cos(\theta_p) \tag{5.5}$$

where

$$r_p = ((y_p - y_v)^2 + (z_p - z_v)^2)^{0.5} \tag{5.6}$$

and

$$\theta_p = \arctan\left(\frac{z_p - z_v}{y_p - y_v}\right). \tag{5.7}$$

The simulated time series of U_{yv} and U_{zv} values at the probe for different positions of the vortex were used to compute 'time-averaged' statistical moments, which were then compared to corresponding measured time-averages. Figure 24 shows typical results along the y-axis at the farthest downstream measuring station; these include mean values of U_z, variances of U_y and U_z, and skewness and flatness factors of U_z.

The agreement between measured and simulated variations of the first and second moments is remarkably close, enhancing our confidence in both the zero-crossing technique used to determine the vortex wandering amplitude and the accuracy of the reconstructed profiles. Differences in the third and fourth moments, which are more sensitive statistical indicators than lower moments and also contain higher uncertainties, are visible, although corresponding values are comparable in magnitude and the variations have comparable shapes. These results further reinforce the observations of Devenport *et al.* (1996) and Heyes *et al.* (2004) that time-averaged statistics near the vortex core are dominated by the influence of vortex wandering.

5.7. *Time dependence of the reconstructed profiles*

The reconstructed profiles of $\widetilde{U}_\theta(\widetilde{r})$ shown in figure 22 were determined using the average or most probable values of $U_{z2}(S)$ and showed a measurable decrease in $\widetilde{U}_{\theta\,\max}$ with increasing free-stream turbulence. In this subsection, we shall examine whether such a decrease could be an artefact of the statistical method employed and whether it is possible for the vortex profiles in grid turbulence to be essentially the same as that in the no-grid case, if not always at least for part of the time. In other words, we shall examine whether there are any instantaneous profiles in grid turbulence that are the same as that in the no-grid case, i.e. whether it is possible for the vortex to evolve in grid turbulence while maintaining its velocity field intact.

To investigate this possibility, we reconstructed the instantaneous outer vortex profile with the highest possible velocity magnitude at each radial position. The method was similar to that described in § 5.2, except that, instead of selecting the average or most probable value of $U_{z2}(S)$ when $U_{z1} = 0$, a likely maximum value $U_{z2}^{(m)}$ was selected. To avoid contamination of the results by outliers, the determination of $U_{z2}^{(m)}$ was subjected to some conditions. To minimize the inclusion of instances at which probe 1 was within the free stream, only values of $U_{z2}(S)$ greater than the value with the peak probability were considered. For the large-grid case, for which two peaks are evident (figure 18), this peak was the one associated with probe 1 being in the core. $U_{z2}^{(m)}(S)$ was determined from the corresponding p.d.f. such that the event $U_{z2}(S) < U_{z2}^{(m)}(S)$ has a 99 % probability of occurring when $U_{z1} = 0$. Then, the radial profile of maximum velocity in the wandering frame was reconstructed as $\widetilde{U}_\theta^{(m)}(\widetilde{r}) \approx U_{z2}^{(m)}(S)$ for $\widetilde{r} = S$.

Profiles of the likely maximum velocity are shown in figure 25(*a–c*). This figure indicates that, as the vortex evolves downstream in grid turbulence, it becomes increasingly implausible for its circumferential velocity profile in the wandering frame to remain comparable to the no-grid profile at the same streamwise position. This observation reinforces the previous observation (figure 22) that free-stream turbulence causes the vortex velocity field to decay.

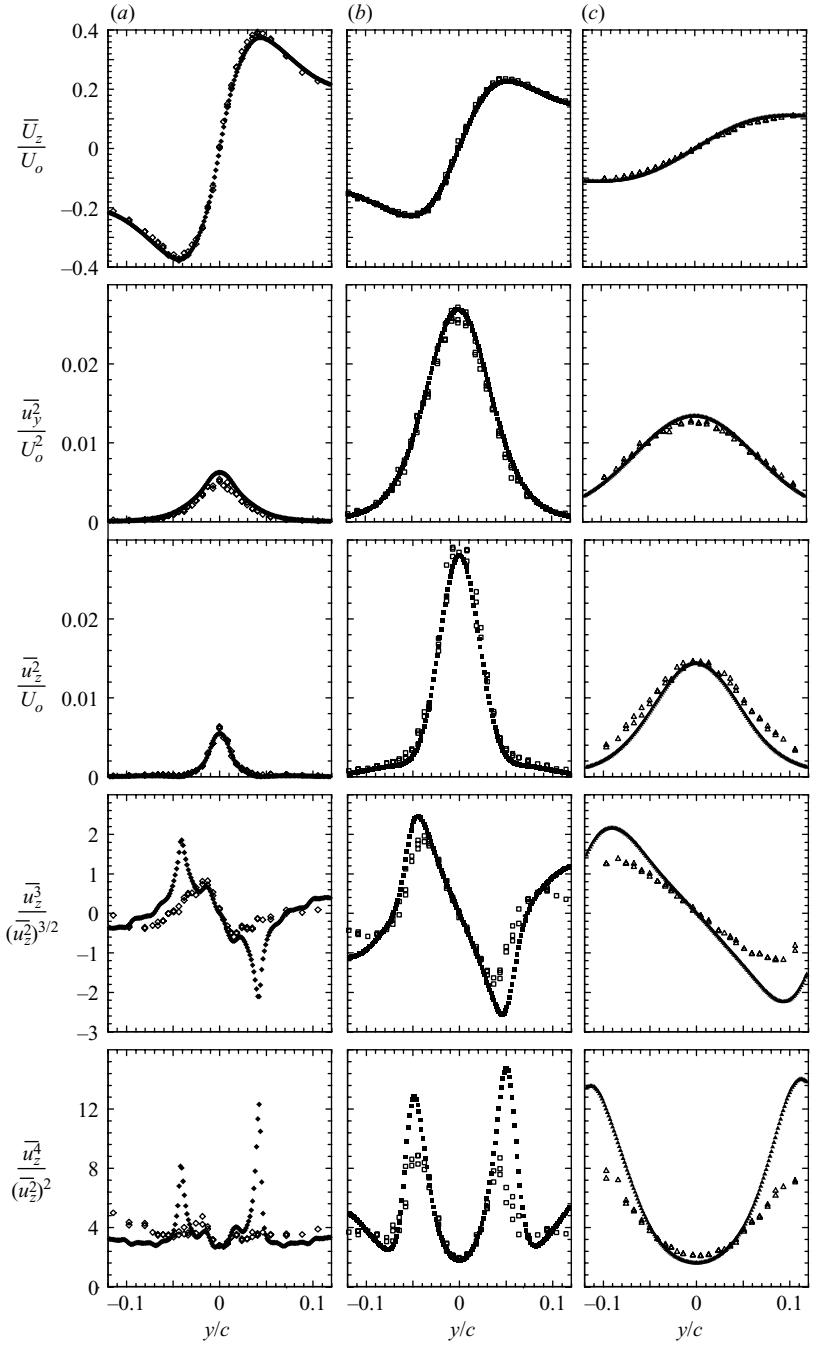

FIGURE 24. Comparison of $\overline{U}_z/U_o$, $\overline{u_y^2}/U_o^2$, $\overline{u_z^2}/U_o^2$, $\overline{u_z^3}/\overline{u_z^2}^{3/2}$, $\overline{u_z^4}/\overline{u_z^2}^2$ determined from measurements (hollow symbols) with values calculated using the reconstructed velocity profile and the measured wandering amplitude (solid symbols) for the no-grid (*a*), small-grid (*b*) and large-grid (*c*) cases at $X/c = 9.75$.

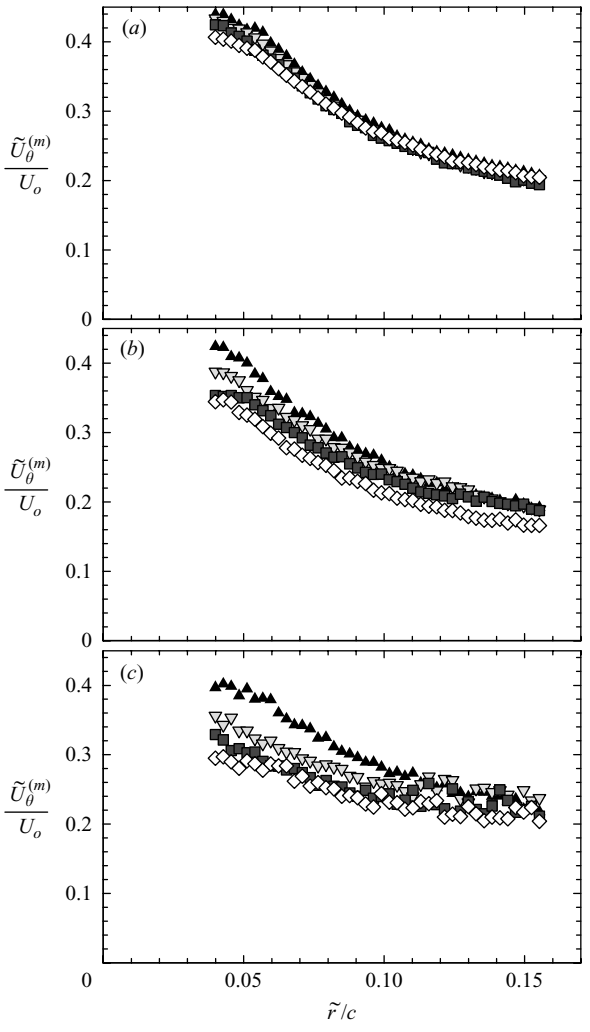

FIGURE 25. Radial profiles of $\widetilde{U}_\theta^{(m)}$ for the (*a*) no-grid, (*b*) small-grid and (*c*) large-grid cases. $X/c = 3.75$ (▲), 5.75 (▽), 7.75 (■) and 9.75 (◇).

6. Discussion

A novel analysis was performed in §4.2 to quantify the amplitude of vortex wandering by determining the joint probability density function (j.p.d.f.) of the vortex position in y and z using the zero crossings of U_y and U_z. It was found that, for the grid-turbulence cases, the j.p.d.f. of the vortex position on the (y, z)-plane was approximately bi-normal, with nearly equal standard deviations in the y- and z-directions and zero correlation coefficient. For the no-grid case, however, because of the relatively coarse spacing of the measurements and the relatively low amplitude of wandering, the effectiveness of the zero-crossing technique was reduced so that it was not possible to either confirm or disprove the existence of a correlation between y- and z-directions of wandering (Devenport *et al.*). The results of the wandering analysis are incompatible with the presence of a dominant helical or sinusoidal vortex motion that would be generated by some instability mechanism. If the motion were helical or sinusoidal, a peak in zero crossings (and a corresponding peak in the j.p.d.f.)

would have been observed at some radial distance from the mean vortex axis, and not on the axis, as found here. It may be further noted that, although an isolated vortex undergoing a sinusoidal ('bending wave') instability would tend to rotate about its own axis and its position would have a j.p.d.f. with a peak on the time-averaged vortex axis, the j.p.d.f. shape would be of the 'Mexican hat' type, rather than Gaussian (Rossow 1999).

The cross-spectra indicated that, although the wandering contained various wavelengths, there existed a dominant wandering wavelength within a range between 2 and 3 wing chords, which was unaffected by changes in the free-stream conditions. This wavelength is far larger than any grid-turbulence length scale and so the source of this wandering motion must be sought elsewhere. It is relevant to note that the dominant wavelength is comparable to both the span of the wing and the distance between its tip and the opposing wind-tunnel wall, and that both of these parameters are independent of free-stream conditions. Although it is possible that this wandering motion is the result of vortex confinement within the test-section walls, a process that has often been modelled by 'mirror vortices' (Rae & Pope 1984), the experiments of Jacquin *et al.* (2001) have indicated that wandering was unaffected by a change in the wind-tunnel geometry (namely the addition of a splitter plate along an aircraft model symmetry plane).

The amplitude of vortex wandering was found to be well described using the standard deviations σ_y and σ_z of the bi-normal distribution in the y- and z-directions. Unlike the wavelength, the wandering amplitude was found to increase both with increasing streamwise distance and increasing free-stream turbulence. A weak directional dependence was observed in the wandering, as σ_y was found to be slightly larger than σ_z, particularly for the large-grid case. However, this small difference can be attributed to the weak anisotropy of the grid turbulence (as mentioned previously, $\overline{u_y^2}$ was slightly larger than $\overline{u_z^2}$). Consistency of the inequalities between the Reynolds normal stresses and the corresponding wandering amplitudes indicates a stochastic contribution to wandering due to transport by free-stream eddies. Hence, it appears that the vortex wandering contains both a deterministic component, possibly associated with the experimental geometry, and a random component associated with the surrounding turbulence.

This study confirms previous observations (Devenport *et al.* 1996; Rokhsaz *et al.* 2000; Baker *et al.* 1974) that the wandering amplitude grows with streamwise distance. Moreover, the wandering was found to have the largest amplitude when the vortex had the lowest peak circumferential velocity (and hence the lowest circulation in the vortex core). This observation further indicates that the wandering was not self-induced; if it were, one would expect that a weaker vortex would wander less than a stronger one.

The average circumferential velocity profile in the wandering frame, reconstructed in § 5, indicates that there is a noticeable impact of free-stream turbulence on the velocity profile of the vortex, with an increase in free-stream turbulence causing an increase in the rate of decay of the peak reconstructed circumferential velocity $\widetilde{U}_{\theta\,\max}$. Interestingly, the radial location $\widetilde{r}_{\theta\,\max}$ at which $\widetilde{U}_{\theta\,\max}$ occurs did not show the corresponding increase that would be required if angular momentum were conserved. Thus, one may conclude that there was a loss of streamwise angular momentum within the vortex core. Such loss may be associated with one or more mechanisms.

A possible explanation for the loss of angular momentum within the vortex core could be sought in possible changes imposed on the vortex formation process by changes in the free-stream turbulence characteristics. The issue here is whether the

initial conditions of the vortex were the same or different for each case investigated. Time-averaged results presented by Bailey *et al.* (2006) have clearly demonstrated that free-stream turbulence had a negligible influence on the lift distribution on the wing, which supports the hypothesis that the time-averaged initial conditions occurring during vortex formation were unaffected by disturbances due to turbulence. Moreover, extrapolation of time-averaged measurements of $r_{\theta\max}$ and $U_{\theta\max}$ towards the wing indicates that all three sets of measurements converged to the same location near the trailing edge (see, for example, figure 5 in the present article or figure 24 in Bailey *et al.* (2006), which has additional data near the wing). This is also reflected in the reconstructed $\widetilde{U}_{\theta\max}$ values through the fit of 5.3, which indicate that $\widetilde{U}_{\theta\max}$ was approximately constant at the trailing edge of the wing.

Although the mean velocity field of the vortex appears to be unaffected by free-stream turbulence during vortex formation, turbulent fluid could become entrained into the vortex core from the free stream or boundary layer, resulting in turbulence within the vortex core and providing a mechanism for turbulent diffusion due to core turbulence. Although comparison of the reconstructed Reynolds stresses to the time-averaged measured Reynolds stresses in figure 24 shows no evidence of additional contributions in the core due to turbulence, the dominance of wandering in the measurements precludes ruling out the existence of turbulence within the core.

Additionally, detrainment of the vorticity at the edge of the core by free-stream eddies, or diffusion due to free-stream turbulence, would lead to transport of vorticity away from the vortex core. Although the stabilizing nature of the rotation within the vortex core is expected to be quite strong, it is possible that vorticity could be transported away from the edge of the core by the very energetic turbulent eddies considered in this study.

The diffusion mechanisms discussed above appear to be the least likely scenarios, based on the evidence provided in the current study. Baker *et al.* (1974) show that a laminar trailing vortex shed from an eliptically loaded wing would decay due to viscosity such that $r_{\theta\max}$ would grow as $(\nu t)^{0.5}$ (ν is the kinematic viscosity and t is time), whereas $U_{\theta\max}$ decreases as $(\nu t)^{-0.25}$. By analogy, one may infer that $r_{\theta\max}$ in a turbulent flow would roughly grow as $(\nu_T t)^{0.5}$ and, likewise, $U_{\theta\max}$ would decrease as $(\nu_T t)^{-0.25}$, where ν_T is some eddy viscosity. Using this argument, one may exclude conventional turbulent diffusion as the source of the vortex decay observed here.

Holzäpfel *et al.* (2003) proposed that angular momentum is transferred from the main vortex to the secondary vortical structures through stretching, in analogy to the energy cascade process in turbulent flows. They observed an initial period of vortex decay, which they interpreted as the result of energy transfer to the secondary structures by stretching of those structures during their formation; they also observed that, following this initial period, the circulation remained nearly constant with time, which they took as evidence that the structures were fully formed. These arguments are supported by figure 23, which shows that the rate of decay of $U_{\theta\max}$ decreases with X/c and that the vortex core circulation seems to approach a constant, as well as the finding of Heyes *et al.* (2004) that, at far downstream distances, the rate of decay of $U_{\theta\max}$ in grid turbulence was small and comparable to that in their no-grid case. On the other hand, one cannot exclude the possibility that the decrease in vortex decay rate observed here is, at least partially, the result of decay of the free-stream turbulence.

Based on DNS results that secondary azimuthally aligned vortical structures tended to arrange themselves in opposing pairs, Marshall & Beninati (2000) proposed the presence of a vortex stripping mechanism, by which large localized radial components

of velocity would convect vortical fluid away from the core. This vortical fluid would then become organized azimuthally, adding to the vorticity of the secondary structures. DNS simulations by Marshall & Beninati (2005) found no evidence of vortex stripping for simulation cases in which the initial condition of turbulence intensity was less than or equal to $0.10U_{\theta\,\max}$. In contrast, in two simulations with higher turbulence intensities ($0.16U_{\theta\,\max}$ and $0.22U_{\theta\,\max}$), Marshall & Beninati (2005) observed that free-stream turbulence caused rapid deformation and breakup of the vortex, even before the secondary structures had time to form. Similar observations were also made by Holzäpfel *et al.* (2003) in their simulations for which the initial conditions had a turbulence intensity of $0.24U_{\theta\,\max}$. It is conceivable that the large-scale free-stream eddies considered in the present investigation could cause intense localized strain of the vortex core, disturbing its axisymmetry and hence introducing an instability mechanism which may lead to breakup and destruction of the vortex. For a crude comparison with the simulations, let us assume that the vortex forms instantaneously at $X/c=0$ with $U_{\theta\,\max}=0.4U_{\infty}$. Then, it follows that, at $X/c=0$, the free-stream turbulence intensity would be approximately $0.17U_{\theta\,\max}$ for the large-grid case and $0.10U_{\theta\,\max}$ for the small-grid case. Taking into consideration differences in the vortex formation process, length scale and rate of turbulence decay rate between simulation and experiment, it seems possible that the present free-stream turbulence is sufficiently strong to initiate the process of vortex destruction.

7. Conclusions

The objective of this study was to observe and document the effects of free-stream turbulence on a wing-tip vortex in the near field. Although recent simulations have provided some interesting insight into the interaction between a vortex and a turbulent free stream, there have been very few experimental studies which have attempted to measure this interaction, mainly because of difficulties arising from the unsteady wandering of the vortex. The present study has overcome these difficulties through the development of an analysis technique which can quantify the vortex wandering and reconstruct the velocity profile of the vortex in the wandering frame of reference. These results were combined to provide a thorough overview of the vortex formation and development in the presence of free-stream turbulence. Time-series analysis indicated that increasing the free-stream turbulence resulted in increasing the amplitude of vortex wandering. The vortex wandering was found to be well represented by a bi-normal distribution of vortex position. Although the amplitude of wandering depended on free-stream conditions, its wavelength was found to be insensitive to changes in the free-stream conditions. Two-point measurements were used to reconstruct the instantaneous velocity profile. Increasing free-stream turbulence was found to increase the rate of decay of the vortex peak circumferential velocity while not significantly affecting the radial distance at which the peak occurs. It is possible that such vortex decay may be attributed to vorticity stripping by secondary coherent structures which form azimuthally around the vortex, transfer of angular momentum from the vortex to these secondary structures during their formation or intense bending and deformation of the vortex caused by its interaction with the free-stream eddies.

The authors acknowledge M. Yaras and B. H. K. Lee for their insightful discussions in the early stages of this work. Additional acknowledgements are due to P. Vukoslavčević for constructing the four-sensor probes used in this study and assisting

with their use and to S. Sjolander for lending us additional anemometers. Financial support was provided by the Natural Sciences and Engineering Research Council of Canada with additional support for S. Bailey provided by the Ontario Graduate Scholarships in Science and Technology program.

REFERENCES

Bailey, S. C. C. 2006 The interaction of a wing-tip vortex and free-stream turbulence. PhD thesis, University of Ottawa.

Bailey, S. C. C., Tavoularis, S. & Lee, B. H. K. 2006 Effects of freestream turbulence on wing-tip vortex formation and near field. *J. Aircraft* **43**, 1282–1291.

Baker, G. R., Barker, S. J., Bofah, K. K. & Saffman, P. G. 1974 Laser anemometer measurements of trailing vortices in water. *J. Fluid Mech.* **65**, 325–336.

Bandyopadhyay, P. R., Stead, D. J. & Ash, R. L. 1991 Organized nature of a turbulent trailing vortex. *AIAA J.* **29**, 1627–1633.

Beninati, M. L. & Marshall, J. S. 2005 An experimental study of the effect of free-stream turbulence on a trailing vortex. *Exps. Fluids* **38**, 244–257.

Bradshaw, P. 1969 The analogy between streamline curvature and buoyancy in turbulent shear flow. *J. Fluid Mech.* **36**, 177–191.

Chow, J. S., Zilliac, G. G. & Bradshaw, P. 1994 Turbulence measurements in the near-field of a wingtip vortex. In *Proc. Turbulence in Complex Flows*, pp. 61–78. ASME.

Comte-Bellot, G. & Corrsin, S. 1966 The use of a contraction to improve the isotropy of grid-generated turbulence. *J. Fluid Mech.* **25**, 657–682.

Corsiglia, V. R., Schwind, R. G. & Chigier, N. A. 1973 Rapid scanning, three-dimensional hot-wire anemometer surveys of wing-tip vortices. *J. Aircraft* **10** (12), 752–757.

Cotel, A. J. & Breidenthal, R. E. 1999 Turbulence inside a vortex. *Phys. Fluids* **11**, 3026–3029.

Devenport, W. J., Rife, M. C., Stergios, I. L. & Follin, G. J. 1996 The structure and development of a wing-tip vortex. *J. Fluid Mech.* **312**, 67–106.

Döbbeling, K., Lenze, B. & Leuckel, W. 1990 Basic considerations concerning the construction and usage of multiple hot-wire probes for highly turbulent three-dimensional flows. *Meas. Sci. Technol.* **1**, 924–933.

Fabre, D. & Jacquin, L. 2004 Viscous instabilities in trailing vortices at large swirl numbers. *J. Fluid Mech.* **500**, 239–262.

Fabre, D., Sipp, D. & Jacquin, L. 2006 Kelvin waves and the singular modes of the lamboseen vortex. *J. Fluid Mech.* **551**, 235–274.

Green, S. I. 1995 *Fluid Vortices*, chap. Wing Tip Vortices, pp. 427–470. Kluwer.

Green, S. I. & Acosta, A. J. 1991 Unsteady flow in trailing vortices. *J. Fluid Mech.* **227**, 107–134.

Gursul, I. & Xie, W. 1999 Origin of vortex wandering over delta wings. *J. Aircraft* **37**, 348–350.

Heaton, C. J. & Peake, N. 2007 Transient growth in vortices with axial flow. *J. Fluid Mech.* **587**, 271–301.

Heyes, A. L., Jones, R. F. & Smith, D. A. R. 2004 Wandering of wing-tip vortices. In *Proc. 12th Intl Symp. on the Applications of Laser Techniques to Fluid Mechanics, Lisbon, Portugal*.

Holzäpfel, F., Hofbauer, T., Darracq, D., Moet, H., Garnier, F. & Gago, C. F. 2003 Analysis of wake vortex decay mechanisms in the atmosphere. *Aerospace Sci. Technol.* **7**, 263–275.

Jacquin, L., Fabre, D., Geffroy, P. & Coustols, E. 2001 The properties of a transport aircraft wake in the extended near field: An experimental study. *AIAA Paper* 2001-1038.

Jacquin, L. & Pantano, C. 2002 On the persistence of trailing vortices. *J. Fluid Mech.* **471**, 159–168.

Lacaze, L., Ryan, K. & Le Dizès, S. 2007 Elliptic instability in a strained batchelor vortex. *J. Fluid Mech.* **577**, 341–361.

Marshall, J. S. 1997 The flow induced by periodic vortex rings wrapped around a columnar vortex core. *J. Fluid Mech.* **345**, 1–30.

Marshall, J. S. & Beninati, M. L. 2000 Turbulence evolution in vortex-dominated flows. In *Nonlinear Instability, Chaos and Turbulence II*, pp. 1–40. WIT Press.

Marshall, J. S. & Beninati, M. L. 2005 External turbulence interaction with a columnar vortex. *J. Fluid Mech.* **540**, 221–245.

Melander, M. V. & Hussain, F. 1993 Coupling between a coherent structure and fine-scale turbulence. *Phys. Rev.* E **48**, 2669–2689.

Miyazaki, T. & Hunt, J. C. R. 2000 Linear and nonlinear interactions between a columnar vortex and external turbulence. *J. Fluid Mech.* **402**, 349–378.

Phillips, W. R. C. 1981 The turbulent trailing vortex during roll-up. *J. Fluid Mech.* **105**, 451–467.

Pope, S. B. 2000 *Turbulent Flows*. Cambridge University Press.

Pradeep, D. S. & Hussain, F. 2006 Transient growth of perturbations in a vortex column. *J. Fluid Mech.* **550**, 251–288.

Rae, W. H. & Pope, A. 1984 *Low Speed Wind Tunnel Testing*, 2nd Ed. John Wiley and Sons.

Rokhsaz, K., Foster, S. R. & Miller, L. S. 2000 Exploratory study of aircraft wake vortex filaments in a water tunnel. *J. Aircraft* **37**, 1022–1027.

Rossow, V. J. 1999 Lift-generated vortex wakes of subsonic transport aircraft. *Prog. Aerospace Sci.* **35**, 507–660.

Sarpkaya, T. & Daly, J. J. 1987 Effect of ambient turbulence on trailing vortices. *J. Aircraft* **6**, 399–404.

Singh, P. I. & Uberoi, M. S. 1976 Experiments on vortex stability. *Phys. Fluids* **19**, 1858–1863.

Spalart, P. R. 1998 Airplane trailing vortices. *Annu. Rev. Fluid Mech.* **30**, 107–138.

Squire, H. B. 1965 The growth of a vortex in turbulent flow. *Aeronaut. Q.* **16**, 302–306.

Sreenivasan, K. R., Tavoularis, S., Henry, R. & Corrsin, S. 1980 Temperature fluctuations and scales in grid-generated turbulence. *J. Fluid Mech.* **100**, 597–621.

Takahashi, N., Ishii, H. & Miyazaki, T. 2005 The influence of turbulence on a columnar vortex. *Phys. Fluids* **17**, 035105.1–035105.14.

Tavoularis, S. 2005 *Measurement in Fluid Mechanics*. Cambridge University Press.

Vukoslavčević, P. V., Petrovic, D. V. & Wallace, J. M. 2004 An analytical approach to the uniqueness problem of hot-wire probes to measure simultaneously three velocity components. *Meas. Sci. Technol.* **15**, 1848–1854.

Wittmer, K. S., Devenport, W. J. & Zsoldos, J. S. 1998 A four-sensor hot-wire probe system for three-component velocity measurements. *Exps. Fluids* **24**, 416–423.